The Astrophysical Journal, 755:47 (19pp), 2012 August 10 doi:10.1088/0004-637X/755/1/47

LOW-FREQUENCY IMAGING OF FIELDS AT HIGH GALACTIC LATITUDE WITH THE MURCHISON WIDEFIELD ARRAY 32 ELEMENT PROTOTYPE

Christopher L. Williams[1], Jacqueline N. Hewitt[1], Alan M. Levine[1], Angelica de Oliveira-Costa[2], Judd D. Bowman[3], Frank H. Briggs[4,5], B. M. Gaensler[5,6], Lars L. Hernquist[2], Daniel A. Mitchell[5,7], Miguel F. Morales[8], Shiv K. Sethi[9], Ravi Subrahmanyan[5,9], Elaine M. Sadler[5,6], Wayne Arcus[10], David G. Barnes[11], Gianni Bernardi[2], John D. Bunton[12], Roger C. Cappallo[13], Brian W. Crosse[10], Brian E. Corey[13], Avinash Deshpande[9], Ludi deSouza[6,12], David Emrich[10], Robert F. Goeke[1], Lincoln J. Greenhill[2], Bryna J. Hazelton[8], David Herne[10], David L. Kaplan[14], Justin C. Kasper[2], Barton B. Kincaid[13], Ronald Koenig[12], Eric Kratzenberg[13], Colin J. Lonsdale[13], Mervyn J. Lynch[10], S. Russell McWhirter[13], Edward H. Morgan[1], Divya Oberoi[13], Stephen M. Ord[10], Joseph Pathikulangara[12], Thiagaraj Prabu[9], Ronald A. Remillard[1], Alan E. E. Rogers[13], D. Anish Roshi[15], Joseph E. Salah[13], Robert J. Sault[7], N. Udaya Shankar[9], K. S. Srivani[9], Jamie B. Stevens[12,16], Steven J. Tingay[5,10], Randall B. Wayth[5,10], Mark Waterson[4,10], Rachel L. Webster[5,7], Alan R. Whitney[13], Andrew J. Williams[17], and J. Stuart B. Wyithe[5,7]
[1] MIT Kavli Institute for Astrophysics and Space Research, Cambridge, MA, USA; clmw@mit.edu
[2] Harvard-Smithsonian Center for Astrophysics, Cambridge, MA, USA
[3] School of Earth and Space Exploration, Arizona State University, Tempe, AZ, USA
[4] Research School of Astronomy and Astrophysics, The Australian National University, Canberra, Australia
[5] ARC Centre of Excellence for All-sky Astrophysics (CAASTRO)
[6] Sydney Institute for Astronomy, School of Physics, The University of Sydney, Sydney, Australia
[7] School of Physics, The University of Melbourne, Melbourne, Australia
[8] Department of Physics, University of Washington, Seattle, WA, USA
[9] Raman Research Institute, Bangalore, India
[10] International Centre for Radio Astronomy Research, Curtin University, Perth, Australia
[11] Center for Astrophysics and Supercomputing, Swinburne University of Technology, Melbourne, Australia
[12] CSIRO Astronomy and Space Science, Epping, Australia
[13] MIT Haystack Observatory, Westford, MA, USA
[14] Department of Physics, University of Wisconsin-Milwaukee, Milwaukee, USA
[15] NRAO, Charlottesville, VA, USA
[16] School of Mathematics and Physics, University of Tasmania, Hobart, Australia
[17] Perth Observatory, Perth, Australia
Received 2012 March 23; accepted 2012 June 5; published 2012 July 25

ABSTRACT

The Murchison Widefield Array (MWA) is a new low-frequency, wide-field-of-view radio interferometer under development at the Murchison Radio-astronomy Observatory in Western Australia. We have used a 32 element MWA prototype interferometer (MWA-32T) to observe two 50° diameter fields in the southern sky, covering a total of ∼2700 deg^2, in order to evaluate the performance of the MWA-32T, to develop techniques for epoch of reionization experiments, and to make measurements of astronomical foregrounds. We developed a calibration and imaging pipeline for the MWA-32T, and used it to produce ∼15′ angular resolution maps of the two fields in the 110–200 MHz band. We perform a blind source extraction using these confusion-limited images, and detect 655 sources at high significance with an additional 871 lower significance source candidates. We compare these sources with existing low-frequency radio surveys in order to assess the MWA-32T system performance, wide-field analysis algorithms, and catalog quality. Our source catalog is found to agree well with existing low-frequency surveys in these regions of the sky and with statistical distributions of point sources derived from Northern Hemisphere surveys; it represents one of the deepest surveys to date of this sky field in the 110–200 MHz band.

Key words: dark ages, reionization, first stars – instrumentation: interferometers – methods: data analysis – surveys

Online-only material: machine-readable table

1. INTRODUCTION

The study of the origin and evolution of the universe draws upon observations of phenomena at a large range of distances and look-back times, connecting the initial conditions probed by the cosmic microwave background to present-day conditions dominated by galaxies and clusters of galaxies. A major chapter of this history has yet to be examined—the chapter that corresponds to redshifts from $z = 1000$ to $z = 6$ and comprises the dark ages and the epoch of reionization (EoR) of the universe. The EoR, in particular, marks a major milestone when the first stars and galaxies formed and reionized the intergalactic medium. It was recognized some time ago that studies of the redshifted 21 cm radio emission from neutral hydrogen would be a promising probe of the EoR (Hogan & Rees 1979; Scott & Rees 1990; Madau et al. 1997). Indeed, the possible existence of extensive regions containing significantly large amounts of neutral hydrogen at redshifts of $z = 15$ to $z = 8$ motivates an interest in developing highly sensitive low-frequency radio telescopes in order to detect the redshifted 21 cm signal. Not long ago it was recognized that a statistical detection of the patchy neutral hydrogen distribution during the EoR should be possible with an array with a modest collecting area and a large field of view (Morales & Hewitt 2004). In the past decade considerable efforts have been made toward this goal, through advances in theoretical modeling of the EoR signature

(see, e.g., Pritchard & Loeb 2011; Morales & Wyithe 2010; Furlanetto et al. 2006 for recent reviews), as well as through the development of new instrumental approaches to measure the redshifted 21 cm signal (see, e.g., Bowman & Rogers 2010; Chippendale 2009; Lonsdale et al. 2009; Parsons et al. 2010; Rottgering et al. 2006; Paciga et al. 2011; S. J. Tingay et al. in preparation).

One particularly daunting challenge for these experiments is emission from foreground astrophysical sources, which is at least two to three orders of magnitude brighter than the redshifted 21 cm signal (in the total intensity as well as in the magnitude of the spatial fluctuations, see, e.g., Shaver et al. 1999; Bernardi et al. 2009; Pen et al. 2009; de Oliveira-Costa et al. 2008). The foreground emission arises mainly from synchrotron and free–free processes, and therefore is highly likely to have an intrinsically smooth radio spectrum. The 21 cm signal, however, is likely to be produced under conditions that vary rapidly with redshift, and, if this is the case, will appear to have rather sharp spectral features. Techniques have been developed to exploit this differing spectral behavior in order to separate and remove the foreground contamination (Furlanetto & Briggs 2004; McQuinn et al. 2006; Bowman et al. 2009; Harker et al. 2009; Liu et al. 2009; Liu & Tegmark 2011). However, any calibration imperfection or instrumental defect has the potential to introduce distortions into measured spectra, and thereby to mix the extremely bright foreground emission with the signal from the redshifted 21 cm signal in ways that are difficult to disentangle (Datta et al. 2010). Thus, an equally daunting challenge is to learn how to calibrate any new instrumentation that is being developed for these observations with extremely high fidelity.

The Murchison Widefield Array (MWA; Lonsdale et al. 2009; S. J. Tingay et al., in preparation) is a new array being constructed to characterize the 21 cm signal during the EoR.[18] In addition to the study of the EoR, other key science goals of MWA include the study of radio transients, the study of the heliosphere and ionosphere, and low-frequency Galactic and extragalactic studies. These four goals and potentially others are addressed by an array made of a large number of small antenna elements that simultaneously give a large collecting area and a large field of view. This is a departure in many ways from a traditional radio array design, with phased arrays of dipoles constituting the fundamental antenna elements, digitization early in the data stream, and full correlation of a large number of baselines. This design promises large improvements with regard to wide-field surveys and detection of the EoR, but, at the same time, it poses new challenges, especially with regard to calibration and imaging of the large field of view and compensation for the effects of the ionosphere. The instrument is currently under construction; work on a 128 element array commenced in early 2012 at the radio-quiet Murchison Radio-astronomy Observatory (MRO) in Western Australia. As a first step in demonstrating the new technologies required for MWA, a 32 element prototype was built at the MRO site prior to the build-out to 128 elements. This prototype system was operated for two years in campaign mode, and underwent a cycle of equipment installation, testing, and redesign as necessary. Beginning in 2010 March, the prototype was used for initial science observations, and has already yielded several results. Oberoi et al. (2011) present findings from an investigation of solar radio emission, and Ord et al. (2010) present wide-field images using a prototype real-time imaging and calibration pipeline. Herein, we also report results based on data obtained during this initial science run.

The goals of the measurements and analysis presented here are to verify the performance of the MWA subsystems and the 32 element prototype array, to explore techniques for future EoR experiments, and to deepen our understanding of the astronomical foregrounds. We observed two overlapping fields at high Galactic latitude, each 50° across. One field was identified for possible EoR studies in the future, and the other was chosen to have a very bright radio source at its center to facilitate calibration. The observations are deep in the sense that they combine data from a large range of hour angles and multiple snapshot images to improve sensitivity and image fidelity; developing such techniques for deep observations is critical for the success of future EoR experiments and other scientific investigations with MWA. We have developed a data reduction pipeline that implements wide-field calibration and imaging algorithms, compensates for the direction-dependent and changing primary beam as different snapshots are combined, and automatically extracts sources from the images. We compare our results directly to the results from other sensitive low-frequency radio surveys in the Southern Hemisphere, and we compare them statistically to the results from surveys carried out in the Northern Hemisphere. We use these comparisons to assess the performance of the MWA prototype and the wide-field imaging and calibration algorithms. We assess the completeness and reliability of our point-source catalog through comparison with these surveys. We make a number of simplifying assumptions in this first phase of analysis; future work will refine the techniques and algorithms until the stringent calibration requirements of EoR experiments with the full MWA can be met.

2. LOW-FREQUENCY RADIO SURVEYS

In this work we make extensive use of the results of previous sensitive low-frequency radio surveys to verify the performance of MWA and to provide external data for calibration. We summarize here the properties of the surveys used in our comparisons.

The Molonglo Reference Catalog (MRC; Large et al. 1981) is the product of a blind survey at 408 MHz that covered nearly all of the southern sky to moderate depth. The catalog covers all right ascensions in the declination range from $-85\overset{\circ}{.}0$ to $+18\overset{\circ}{.}5$, excluding the area within 3° of the Galactic plane. The observations were conducted with the Molonglo Radio Telescope in a 2.5 MHz wide band with a synthesized beam of $2\overset{\prime}{.}62 \times 2\overset{\prime}{.}86\,\mathrm{s}(\delta + 35\overset{\circ}{.}5)$ in width. The MRC has a stated completeness limit of 1 Jy, although it contains sources down to a flux of ∼0.7 Jy.

At frequencies below 408 MHz, there have been many targeted observations of known sources in the southern sky. The Culgoora Circular Array (Slee 1995) was used to observe Galactic and extragalactic sources selected from existing higher frequency surveys. The observations were made at frequencies of 80 MHz and 160 MHz. The beam size was $3\overset{\prime}{.}70 \times 3\overset{\prime}{.}70\mathrm{s}(\delta + 30\overset{\circ}{.}3)$ at 80 MHz, and $1\overset{\prime}{.}85 \times 1\overset{\prime}{.}85\,\mathrm{s}(\delta + 30\overset{\circ}{.}3)$ at 160 MHz. The limiting flux density was 4 Jy at 80 MHz, and 2 Jy at 160 MHz. However, only a small patch of sky around each selected source was imaged. Although flux density uncertainties are not directly reported in this list, Slee (1977) notes that the standard deviation in the flux density for sources measured with the Culgoora array is ∼13% for the brightest sources, and ∼39%

[18] Additionally, the MWA has been designated an official precursor instrument for the Square Kilometre Array (SKA).

for the faintest sources, with a potential systematic flux scale depression of ∼10%. Similarly, Jacobs et al. (2011) present results from PAPER, an array of east–west polarized dipoles, that were obtained over the 110–180 MHz band. The results were derived from multifrequency synthesis maps of the entire sky south of a declination of 10° having a resolution of 26′. A sample of 480 sources with fluxes greater than 4 Jy in the MRC were identified and measured in these PAPER maps. Jacobs et al. (2011) find a 50% standard deviation in their fluxes relative to values obtained from the MRC and Culgoora source lists. They quote a flux limit of 10 Jy for the sources in their catalog.

Surveys which primarily cover the northern sky have also been carried out at low frequencies. The most extensive wide-field uniform survey near our observing frequency of 150 MHz is the 6C survey (Baldwin et al. 1985; Hales et al. 1988, 1990, 1991, 1993a, 1993b). The 6C survey covered the northern sky above declination 30° with a sensitivity of 200 mJy; the angular resolution was $4\farcm2 \times 4\farcm2 \csc \delta$. The 7C survey (Hales et al. 2007) covers 1.7 sr of the northern sky to a greater depth and at higher resolution than the 6C survey. We have chosen to use the 6C survey for comparison to our results in this paper because it covers a somewhat larger sky area, and has served as the basis for other investigations of EoR foregrounds (in particular, Di Matteo et al. 2002). At lower frequencies, Cohen et al. (2007) have used the Very Large Array (VLA) 74 MHz system to perform a survey of the sky north of declination $\delta = -30°$. This survey, known as the VLA Low-Frequency Sky Survey (VLSS), produces maps with an 80″ angular resolution that achieve a typical rms noise level of 100 mJy beam^{-1}. Each VLSS image is $14° \times 14°$ across in order to fully image the VLA primary beam, which has an FWHM diameter of $11\fdg9$. Cohen et al. (2007) performed a blind source extraction on the VLSS maps and produced a source catalog of 68,311 radio sources above a significance level of 5σ. They quote a 50% point-source detection limit of 0.7 Jy beam^{-1}.

There are also several ongoing efforts to perform low-frequency blind surveys. Pandey (2006) presents results from a survey that used the Mauritius Radio Telescope (MRT) to image ∼1 sr of the sky at 151 MHz and to thereby produce a catalog of 2782 sources.[19] The deconvolved images achieve an angular resolution of $4' \times 4\farcm6\,\mathrm{s}(\delta + 20\fdg14)$ and an rms noise level of approximately 300 mJy beam^{-1} (Nayak et al. 2010). The TIFR GMRT Sky Survey (TGSS; Sirothia et al. 2011) is producing a 150 MHz survey of the sky at declinations above −30°. Each pointing covers ∼7 deg^2 and yields a map that reaches an rms noise of ∼8 mJy beam^{-1} at an angular resolution of ∼20″. The flux density scales of the maps are limited by systematic errors and have relative errors of 25%. As of 2012 January, the TGSS Web site[20] reports results from images of approximately 2600 deg^2 of the southern sky. The LOFAR Multifrequency Snapshot Survey (LOFAR-MSSS[21]; G. H. Heald et al., in preparation) is using the LOFAR instrument to survey 20,000 deg^2 of the sky with an angular resolution of $\lesssim 2'$, and a sensitivity better than 15 mJy beam^{-1}. The survey will cover between 30 MHz and 170 MHz, with a 16 MHz instantaneous bandwidth.

For completeness we note that additional low-frequency surveys include the Sydney University Molonglo Sky Survey (843 MHz; Bock et al. 1999), the Miyun Survey (232 MHz; Zhang et al. 1997), and the Levedev Physical Institute Survey (102.5 MHz; Dagkesamanskiĭ et al. 2000). We have not extensively compared our results to results from these surveys.

Low-frequency surveys have also been used to study the distribution of spectral indices of radio sources. De Breuck et al. (2000) used results from the MRC and from the Parkes-MIT-NRAO 4.85 GHz survey (PMN; Wright et al. 1994, 1996; Griffith & Wright 1993; Griffith et al. 1994, 1995; Condon et al. 1993; Tasker et al. 1994) to study the distribution of spectral indices of sources in the southern sky. They also carried out similar comparisons of the results from the Westerbork Northern Sky Survey (325 MHz; Rengelink et al. 1997) and the Texas Survey (365 MHz; Douglas et al. 1996) with results from the NRAO VLA Sky Survey (1.4 GHz; Condon et al. 1998) in the Northern Hemisphere. The spectral index distributions showed significant differences between samples selected at low frequencies and samples selected at high frequencies. The combined MRC-PMN source list was also used to generate a sample of ultra-steep spectrum (USS) sources.

In Section 7.1, we carry out source-by-source comparisons of our survey results to those of the MRC, the Culgoora flux density measurements, the PAPER flux density measurements, and the TGSS. There is no overlap at present between our survey and the Mauritius survey, but comparisons should become possible when the analysis of the Mauritius data is completed. We also carry out statistical comparisons of our survey results to those of the 6C survey by comparing source counts, and to the De Breuck et al. (2000) spectral index catalogs by comparing spectral index distributions.

3. THE MWA-32T INSTRUMENT

The Murchison Widefield Array 32-Tile prototype (MWA-32T) was built and operated for the purpose of verifying the performance of MWA subsystems in preparation for building a larger, more capable array. As noted above, construction of a 128 tile array has commenced and is expected to be complete later this year (2012). We summarize the design here; the reader is referred to Lonsdale et al. (2009) and S. J. Tingay et al. (in preparation) for more detailed descriptions.

The MWA-32T was designed to cover a frequency range from 80 MHz to 300 MHz, with an instantaneous bandwidth of 30.72 MHz at a spectral resolution of 40 kHz. The array consisted of 32 antenna tiles, which served as the primary collecting elements of the array. The tiles are designed to have an effective collecting area larger than 10 m^2 in the MWA frequency band, and to provide a steerable beam which can be pointed up to 60° from zenith while maintaining a system temperature which is dominated by sky noise within the MWA band. The primary beam of the tiles is frequency and position dependent, with an FWHM size at zenith of roughly $25°/(\nu/150\,\mathrm{MHz})$. Each tile consists of 16 dual-polarization, active dipole antennas laid out over a metal mesh ground screen in a 4 × 4 grid with a 1.1 m center-to-center spacing. Each dipole antenna consists of vertical bowtie elements that feed a pair of integrated low-noise amplifiers located within a tube at the juncture of the orthogonal arms of the dipole. The antennas are designed to have low horizon gain to reduce terrestrial radio frequency interference (RFI) contamination, and to have a low manufacturing cost.

The signals for the two polarizations are processed in parallel. For each polarization, the signals from the 16 dipoles on each tile are carried over coaxial cable to an analog beamformer, where they are coherently summed to form a single tile beam. A system of switchable analog delay lines is used to apply an independent time delay to each of the dipole signals, allowing

[19] Electronic catalogs are available at http://www.rri.res.in/surveys/MRT.
[20] http://tgss.ncra.tifr.res.in/150MHz/tgss.html
[21] http://www.astron.nl/radio-observatory/lofar-msss/lofar-msss

the tile beam to be steered on the sky. The delay lines employ a series of five switchable traces, each differing by a factor of two in length, with the shortest trace introducing a nominal delay of 435 ps. This allows for 32 discrete delay settings for each of the input signals. The discretization of the delays implies that the primary beam can only be steered in discrete steps, and so can only coarsely track a sky field. The summed signal is amplified and sent over coaxial cables to the MWA digital receiver for digitization.

Each MWA digital receiver node services eight tiles. The 16 received signals are first subjected to additional filtering and signal conditioning for low-frequency rejection, anti-aliasing, and level adjustment. The signals are then digitized at baseband by eight dual 8 bit analog-to-digital converter (ADC) chips operating at a sampling rate of 655.36 MHz. The data stream from each ADC is fed to a digital polyphase filterbank (PFB) implemented in FPGA hardware which produces 256 frequency channels, each 1.28 MHz wide. A sub-selection of 24 of these channels (a bandwidth of 30.72 MHz) is transmitted via optical fiber to the correlator.

At the correlator, the data streams from each receiver are processed by a second stage PFB to obtain a frequency resolution of 10 kHz. The signals are then cross-multiplied to produce a 3072 channel complex spectrum for each of the 2080 correlation products. These comprise the four polarization products for all pairs of tiles as well as the autocorrelations. The visibilities are averaged into 40 kHz wide channels and integrated for 50 ms due to output data rate constraints. During the 32T observing campaign described in this work, the correlator was operating at a 50% time duty cycle due to hardware limitations. The visibilities are captured and averaged into 1 s integrations before being written to disk.

4. OBSERVATIONS

Observations were conducted with the MWA-32T in 2010 March during a two-week campaign (X13) when personnel were present on-site to operate the instrument. Data were taken in three 30.72 MHz sub-bands centered at 123.52 MHz, 154.24 MHz, and 184.96 MHz in order to give (nearly) continuous frequency coverage between ∼110 MHz and ∼200 MHz. During the observations, the beamformers were used to steer the beam in steps as the fields crossed the sky. This stepped steering is a consequence of the discretization of the analog delay lines in the beamformer. The typical sequence was to steer the beam to a new position, observe at a particular frequency for five minutes (without tracking), and then steer the beam again. Thus, the measurements can be considered to be a series of short drift scans.

The observing time was divided between two fields. One field was centered on the bright extragalactic source Hydra A at R.A.(J2000) = $9^h18^m6^s$, decl.(J2000) = $-12°5'45''$ to facilitate calibration. The other covered the EoR2 field, centered at R.A.(J2000) = $10^h20^m0^s$, decl.(J2000) = $-10°0'0''$. The EoR2 field is one of two fields at high Galactic latitude that have been identified by the MWA Collaboration as targets for future EoR experiments. It also had the advantage of being above the horizon at night during the observing campaign. Although the centers of the Hydra A and EoR2 fields are separated by 15°.3, there is considerable overlap between them since the half power beam width of the primary beam is ∼25° at 150 MHz. A total of 61 ∼ 5 minute scans of the Hydra A field and 248 scans of the EoR2 field were obtained in interleaved sequences over the course of the observing sessions. Table 1 gives a journal of the observations.

Table 1
Journal of Observations

Field	Frequency (MHz)	Date	Number of Scans	Observation[a] Time (minutes)
EoR2	123.52	2010 Mar 24	35	208
		2010 Mar 28	26	154
	154.24	2010 Mar 22	35	208
		2010 Mar 26	18	107
		2010 Mar 28	10	59
	184.96	2010 Mar 21	35	208
		2010 Mar 25	35	208
		2010 Mar 26	18	106
		2010 Mar 29	36	214
Hydra A	123.52	2010 Mar 24	8	39
		2010 Mar 28	7	34
	154.24	2010 Mar 22	8	39
		2010 Mar 26	5	24
		2010 Mar 28	3	15
	184.96	2010 Mar 21	8	39
		2010 Mar 25	8	39
		2010 Mar 26	5	24
		2010 Mar 29	9	44

Note. [a] The effective integration time is less than half of this observation time due to the 50% duty cycle of the correlator and additional flagging.

5. DATA REDUCTION STRATEGY

5.1. Instrumental-gain Calibration

The MWA antenna tile architecture poses several nontraditional calibration issues due to both the nature of the primary beam and the wide field of view. The primary beam is formed by the summation of beamformer-delayed zenith-centered dipole responses. The beamformer delays are periodically changed to track a field across the sky. Although this moves the center of the primary beam as intended, the overall shape of the beam changes as well. For a given set of beamformer delays, the beam is fixed relative to the tile, and therefore moves relative to the sky as the Earth rotates. As a further complication, the time and direction dependence of the primary beam response is different for the two polarizations of the crossed dipoles in the array. This leads to apparent polarization in inherently unpolarized sources due to the different responses in the two orthogonal dipole polarizations unless the appropriate corrections are applied in the analysis procedure.

Methods for measuring and calibrating the primary beam have been developed for the full MWA system by Mitchell et al. (2008), who plan to use a real-time system (RTS) to calibrate and image MWA data. Their method performs a calibration of the instrument in real time, solving for direction- and frequency-dependent gains for each antenna based on the simultaneous measurement of multiple known bright sources across the field of view. This method was developed for use in a 512-tile array, where the instantaneous sensitivity and uv-plane coverage enable the measurement of several hundred sources in each 8 s iteration (Mitchell et al. 2008). Ord et al. (2010) have successfully demonstrated the use of a modified version of the RTS in order to calibrate and image data from the MWA-32T. However, the reduced sensitivity of the MWA-32T array makes this full calibration challenging. For the MWA-32T system, the data rate is sufficiently low that real-time calibration and imaging are not necessary, and the raw visibility data can be captured and stored. We have chosen to pursue an alternative data reduction pipeline based on more traditional calibration and

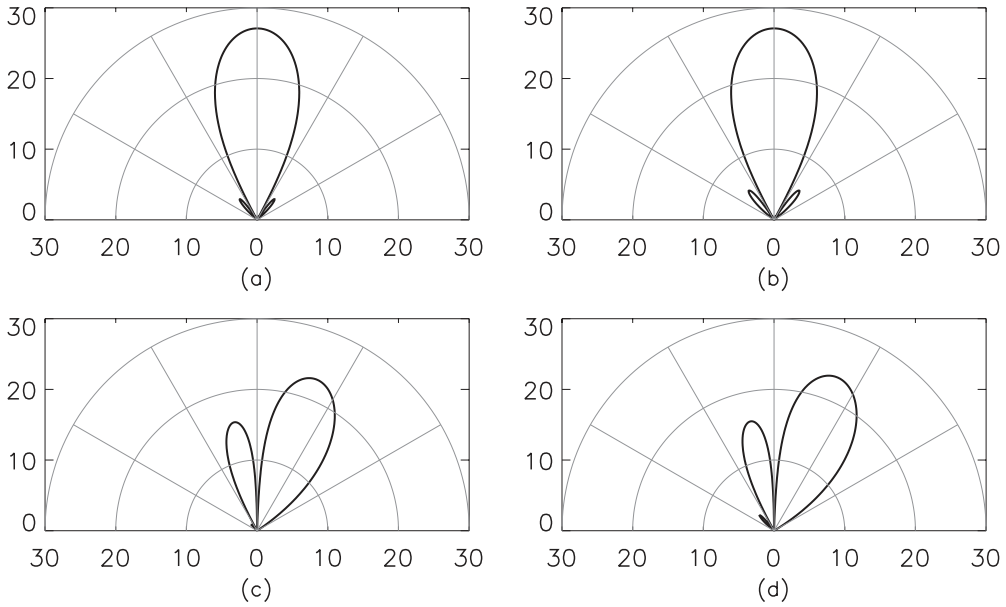

Figure 1. West–east cuts through simulated MWA antenna tile patterns for a zenith ((a), (b)) and a 28° easterly pointing ((c), (d)) at 150 MHz. Panels (a) and (c) show the X-polarization dipole power response pattern, while panels (b) and (d) show the Y-polarization power response pattern. The scale is logarithmic, with arbitrarily normalized decibel units. The polarization-dependent gain structure is clearly visible in the sidelobes.

imaging software, which allows us to use the full visibility data set in order to perform a detailed investigation of the calibration and imaging performance of the MWA-32T instrument.

Without the ability to directly measure the primary beam for each tile, we instead assume a model and use it to account for the instrumental-gain direction dependences. Knowledge of the primary beams is also needed for an optimized weighting of the maps when combining them to obtain deeper maps (see Section 6.4). It is likely that precise characterization of individual tile beams will be necessary to achieve dynamic range sufficient for accurate foreground subtraction and EoR detection, but this is not attempted in the work described herein.

For present purposes, we assume that the polarized primary beam patterns are identical across all tiles, and can be modeled by simply summing together the direction-dependent complex gains of the individual dipoles in the tile, i.e., mutual coupling between elements and tile-to-tile differences are ignored. We model the complex beam patterns of an isolated individual dipole for both the north–south (Y) and east–west (X) electric field polarizations using the `WIPL-D Pro`[22] electromagnetic modeling software package. A tile beam pattern is then computed by summing the 16 dipole responses with the dipoles assumed to be at their nominal locations in a tile and with the individual responses modified by the nominal amplitudes and phases introduced by the beamformer for the given delay settings. Figure 1 shows cuts through power patterns (square modulus of the complex beam) at zenith and at a pointing direction 28° east of zenith for both the X and Y polarizations. Model beam patterns were calculated at frequency intervals of 2 MHz, since they vary significantly across the MWA frequency band.

We assume that this model fully describes the direction dependence of each tile. We do, however, allow for a different overall, i.e., direction-independent, complex gain for each tile. We follow the Jones matrix formalism as presented by Hamaker et al. (1996). The instrumental model then takes the following form for a single tile at a single frequency:

$$\mathbf{v}_A = \mathbf{G}_A \mathbf{B} \mathbf{e}_A, \tag{1}$$

where

$$\mathbf{e}_A = \begin{pmatrix} e_x \\ e_y \end{pmatrix} \tag{2}$$

is the incident electric field at tile A, decomposed into linear E–W and N–S polarizations,

$$\mathbf{v}_A = \begin{pmatrix} v_x \\ v_y \end{pmatrix} \tag{3}$$

is the vector of measured antenna voltages,

$$\mathbf{G}_A = \begin{pmatrix} g_{A,x} & 0 \\ 0 & g_{A,y} \end{pmatrix} \tag{4}$$

is the matrix of direction-independent complex gains for an antenna, and

$$\mathbf{B} = \begin{pmatrix} b_x(\theta, \phi) & 0 \\ 0 & b_y(\theta, \phi) \end{pmatrix} \tag{5}$$

is the matrix of direction- and frequency-dependent but tile-independent gains due to the primary beam shape (we represent spatial coordinates with θ and ϕ). We neglect the feed-error "D" matrix of Hamaker et al. (1996); in other words we assume that the sensitivity of the X-polarization response of a dipole to Y-polarization radiation (the cross-polarization) is zero, and vice versa. This is likely to be a good approximation since ideal dipoles have zero cross-polarization by definition. In reality, various effects, such as the finite thickness of our dipole elements, interactions between structures in neighboring dipoles, or projection effects may produce a nonzero cross-polarization response. In this paper we restrict our imaging and analysis to these two senses of linear polarization and their combination as total intensity. Errors caused by neglecting cross-polarization effects are second order in the small off-diagonal elements of the D matrix.

The strategy we adopt for the data reduction is first to analyze short snapshots wherein the settings in the analog beamformer were static so that the primary beam pattern can be taken as constant over the duration of each snapshot, and any gain

[22] http://www.wipl-d.com

changes due to the sidereal motion of the sky relative to the beam can be neglected. In this regime, the direction-dependent gain can be factored out of the response and corrected in the image plane in the resulting map. Under this approximation, we are able to use standard tools for radio astronomical data analysis for much of the processing. Finally, the frequency dependences of the overall antenna complex gains are in principle determined by modeling the summed spectra of the bright sources in the field used in the calibration.

Standard calibration procedures rely on being able to observe a field containing a strong source with easily modeled structure that substantially dominates the visibilities. For the two fields presented in this work, Hydra A is the strongest source in the field. Lane et al. (2004) present low-frequency images that show that while it is quite extended at the VLA's resolution, most of the flux is contained within a region that is a few arcminutes in radius. Since this extent is smaller than the angular resolution of MWA-32T, we were able to treat Hydra A as a point source in our calibration analysis. One might expect that for a large field-of-view instrument such as MWA, we would also need to include several or even many additional strong sources in the calibration model with known direction-dependent gains. We therefore experimented with calibration models that included several point sources in addition to Hydra A, but we found that the complex tile gain solutions were not significantly changed. We therefore simply used Hydra A as the only calibration source in subsequent analysis. It should be noted that this is a potential source of error.

5.2. Ionosphere

At the low radio frequencies of MWA, position- and time-dependent variations in the electron density of the ionosphere cause variations in propagation times, which appear in the visibility data as frequency- and time-dependent phase shifts. For the short baselines of the MWA-32T, these variations are, except at times of extreme ionosphere disturbance, refractive in effect, i.e., they simply cause apparent changes in the positions of point sources on the sky. These position shifts may be different in different directions, especially over a wide field such as that of the MWA, and consequently may lead to distortions in the derived images.

Ionospheric effects have been quantified by studies with other low-frequency interferometers. Baldwin et al. (1985), using the Cambridge Low-Frequency Synthesis Telescope at 150 MHz, found that the ionosphere typically caused 5° (rms) phase variations on 1 km baselines on sub-day timescales, which were uncorrelated from day to day. They also remarked that ionospheric irregularities on large spatial scales, most likely related to the day–night cycle and strongly correlated from one day to the next, could induce apparent position shifts of sources of up to 20′. Kassim et al. (2007) found, with the VLA operating at 74 MHz, that during times of moderate ionospheric disturbance relative position variations on short timescales across a 25° field of view were at most 2′. Similarly, Parsons et al. (2010), using observations of bright sources with the PAPER array at 150 MHz, found short-term small (typically less than 1′) position offsets that were not correlated from day to day, and long-term large (up to 15′) position offsets which were correlated from day to day, and were mainly in the zenith direction.

In our analysis, we average snapshots taken with the center of the field within several hours of the local meridian over a period of eight days. The results in the papers cited above suggest that uncorrelated short-term variations in source directions will be significantly smaller than our beam size of ∼15′ and, furthermore, that they will tend to average out when images derived from individual snapshots are combined. We therefore neglect them. Long-term correlated variations in source directions may be comparable to our beam size, and may not average to zero as we combine snapshot images. However, our calibration strategy, described in Section 5.1, will tend to remove any ionospheric offset at the position of Hydra A through the phase terms in the direction-independent gain solutions. It is possible, depending on the behavior of the ionosphere during the present observations, that long-term differential position shifts of several arcminutes might be present in our final images. We investigate this possibility through comparisons of the positions of our extracted sources with source positions listed in published catalogs.

Our neglect of short-term ionospheric effects is justified only because of the small baselines (<350 m) of the MWA-32T array. For the longer baselines (∼3 km) of the full MWA, we believe that these effects will need to be corrected to achieve the dynamic range required for many of the science goals.

6. REDUCTION PIPELINE

6.1. Initial Processing and Editing

We developed a calibration and imaging pipeline based on the NRAO Common Astronomical Software Applications[23] (CASA) package and additional tools that we developed in Python and IDL. The pipeline uses a series of short observations to generate "snapshot" images which are weighted, combined, and jointly deconvolved to produce final integrated maps.

In the first stage of the pipeline, the visibilities were averaged over 4 s intervals and converted from the MWA instrumental format into UVFITS files. The MWA-32T correlator does not perform fringe-stopping (the correlation phase center is always at zenith), so phase rotations were applied to the visibilities to track the desired phase center. As a part of this process, data corrupted by RFI were flagged for later exclusion from the analysis. The data were then imported into CASA. Additional editing was done to flag data affected by known instrumental problems or RFI. Approximately 25% of the data were flagged at this stage, mainly because a problem in the data capture software corrupted 480 of the 2080 correlation products.

6.2. Calibration of Antenna Gains

Calibration was performed separately for each snapshot with CASA, using Hydra A as the gain and phase reference (as discussed in Section 5.1). Although Hydra A was not at the center of the primary beam during observations of the EoR2 field, it was still strong enough to substantially dominate the visibilities. Model visibilities were calculated using a point-source model for Hydra A, assuming an unpolarized flux of unity. The overall frequency-dependent flux scale of the data was set at a later point, along with a correction for the direction-dependent gain. Time-independent channel-by-channel gain factors were calculated for each tile using the task `bandpass`. After this was done and the visibilities corrected for the gain factors, time-dependent overall tile gain factors were calculated on a 32 s cadence using the task `gaincal`. The factors determined in the two tasks give the frequency- and time-dependent $g_{A,x}$ and $g_{A,y}$ terms of Equation (4).

[23] http://casa.nrao.edu

The $g_{A,x}$ and $g_{A,y}$ terms were examined for temporal stability and spectral smoothness; regions where deviations were apparent were flagged. Such deviations were rare, and an important outcome of this analysis is the recognition that the MWA antenna gains are quite stable over frequency and time. In fact, the gains even tended to be stable from one day to the next. However, some complicated variations in gain as a function of frequency were identified. These were associated with damaged cables and connectors that have since been replaced or repaired.

6.3. Snapshot Imaging

The data from each snapshot were subdivided into 7.68 MHz wide frequency bands, and multifrequency synthesis imaging was performed for each snapshot using the CASA task clean. Images were made with a 3′ cell size over a $\sim 51^\circ \times \sim 51^\circ$ patch of sky in order to cover the majority of the main lobe of the primary beam. The "XX" and "YY" polarizations were imaged separately. Conversion to the standard Stokes parameters was not performed at this stage, since, as discussed in Section 5.1, the gains for the two polarizations have different direction dependence. The "w-projection" algorithm (Cornwell et al. 2008) was used to correct for wide field-of-view effects, and to produce an image with an approximately invariant point-spread function (PSF) in each of the snapshot images. The images were deconvolved using the Cotton–Schwab CLEAN algorithm (see Schwab 1984) down to a threshold of 1% of the peak flux in the image.

A position-dependent "noise" map was also computed for each of the 7.68 MHz wide snapshot images by selecting a 64 pixel by 64 pixel window around each pixel in the image and fitting a Gaussian to the central 80% of a histogram of the pixel values. This procedure was employed because of the high point-source density in these maps. Throughout much of the area of these maps, it was impossible to identify a source-free region from which to estimate the background noise fluctuations, and the presence of sources artificially skewed the noise estimates calculated strictly as the rms of the pixel values. We found that this clipped histogram fitting procedure provided a more robust estimate of the rms of the background noise. These noise maps were smoothed on a 1° scale to remove local anomalies introduced by extended or clustered sources. However, despite these procedures, some areas, particularly in especially crowded regions, still had anomalously high-noise estimates.

As discussed above, each snapshot was only ∼5 minutes in duration, and was obtained while the delay line settings in the analog beamformers were fixed. This allowed us to model the primary beam pattern of each tile as fixed relative to the sky for the duration of the snapshot. Our calculated model beams for each polarization formed the frequency-dependent $b_x(\theta, \phi)$ and $b_y(\theta, \phi)$ terms of Equation (5). These terms are time dependent only in that they are different for each snapshot.

6.4. Snapshot Combination and Joint Deconvolution

Deeper images were obtained by combining snapshot maps from a particular 7.68 MHz wide band according to

$$I_{\rm dirty}(\theta, \phi) = \frac{\sum_i \frac{D_i(\theta,\phi)B_i(\theta,\phi)}{\sigma_i^2(\theta,\phi)}}{\sum_i \frac{B_i^2(\theta,\phi)}{\sigma_i^2(\theta,\phi)}}, \quad (6)$$

where $I_{\rm dirty}$ is the integrated, primary beam corrected, dirty map, the snapshots are distinguished by index i, D_i is a snapshot dirty map, B_i is the primary beam calculated for that snapshot, and σ_i is the fitted rms noise obtained from the noise map for snapshot i. This combination optimizes the signal-to-noise ratio (S/N) of the final image. Beam patterns are calculated independently for each 7.68 MHz channel. The same weighting scheme was used to combine the "clean components" and residual maps of the individual snapshots.

A variant of the Högbom CLEAN algorithm (Högbom 1974) was used to further deconvolve the integrated residual maps, using a position-dependent PSF calculated using the same weighting scheme:

$$P_{{\rm integrated},\,j}(\theta, \phi) = \sum_i \frac{B_i(\theta, \phi)B_i(\theta_j, \phi_j)P_i(\theta - \theta_j, \phi - \phi_j)}{\sigma_i^2(\theta, \phi)}, \quad (7)$$

where $P_{{\rm integrated},\,j}$ is the PSF for a source at position (θ_j, ϕ_j), B_i is the primary beam pattern for the ith snapshot with a PSF given by P_i, and the peak of the function is normalized to unity. CLEAN components were selected by choosing the pixel in the residual map with the largest S/N (determined by dividing the residual map by its noise map). The PSF was scaled to a peak of 10% of the flux of the pixel. The images were restored with a Gaussian beam determined by a fit to the weighted average of the individual snapshot PSFs at the field center.

6.5. Averaging

In order to increase the S/N and image fidelity for source detection and characterization, the individual 7.68 MHz maps, after deconvolution and restoration, were averaged together. An approximate flux scale for the maps was first set by scaling the surface brightness of the maximum pixel at the location of Hydra A to a value of $296 \times (\nu/150\,{\rm MHz})^{-0.91}$ Jy beam^{-1} (this model was derived from fitting a power law to other low-frequency measurements). For each field, 30.72 MHz bandwidth maps centered at 123.52 MHz, 154.24 MHz, and 184.96 MHz were each made from four 7.68 MHz maps. Before averaging, the 7.68 MHz map fluxes were scaled to the averaged map frequency using an assumed spectral index of $\alpha = -0.8$ (where $S \propto \nu^\alpha$). The averages were computed in a weighted sense using the integrated primary beam weights from each map. A full-band (92.16 MHz bandwidth) weighted average map was made from the three 30.72 MHz bandwidth maps after scaling them to a common reference frequency of 154.24 MHz, again using a spectral index of $\alpha = -0.8$. The portion of each field within 25° of the field center was used for the subsequent analysis.

6.6. Source Extraction

Sources were identified in each full-band, i.e., 92.16 MHz wide, averaged map using an automated source extraction pipeline. The first step of this pipeline was the calculation of a position-dependent noise map using the method described in Section 6.4. The full-band map was then divided by the noise map to produce an S/N map. An iterative process then was initiated by identifying contiguous regions of pixels above a certain S/N detection threshold and, for each such region, defining a fitting region that extended beyond the set of connected pixels by several synthesized beamwidths. A two-dimensional Gaussian fit was performed on the corresponding region in the full-band map. The parameters determined in each fit included the background level, peak position, peak amplitude, major-axis width, minor-axis width, and position angle. If the fit converged to a Gaussian centered within the fitting region, then the source was subtracted from the map, and

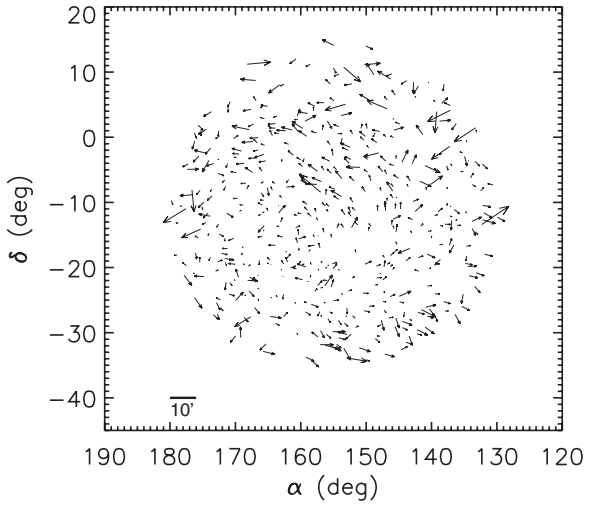

Figure 2. Spatial offsets between the positions of MWA sources in the EoR2 field and matched sources in the Molonglo Reference Catalog (Large et al. 1981). An overall coordinate system shift has been removed.

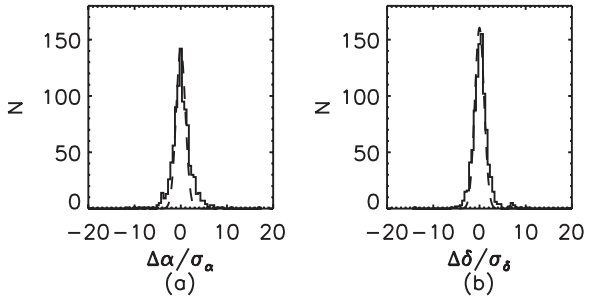

Figure 3. Histograms of the normalized right ascension, α (a) and declination, δ (b) errors for the extracted MWA sources relative to matched sources in the Molonglo Reference Catalog (Large et al. 1981). The standard deviations, σ_α, and σ_δ, are calculated following Condon (1997) with the simplifying assumption of circular source geometry. Assuming Gaussian error properties, the residual distribution should approximate a standard normal distribution, which is overplotted with a dashed line. Hydra A is omitted from the histograms.

the extracted source parameters were recorded. After fitting all regions identified for a certain S/N level, the detection threshold was reduced and the process was repeated. Regions above the detection threshold for which a fit failed to converge are refit in subsequent iterations at lower detection thresholds (where the fitting regions are typically larger in size). For completeness, sources were extracted down to a detection S/N threshold of 3. It should be noted that in this fitting procedure, each region that is fit by a single two-dimensional Gaussian is taken to correspond to a separate source. Sources that are too close together to be resolved into separate components will be fit with a single component and erroneously taken to be a single source that is a "blend" of the two components.

Sources that were identified in the full-band average map were then extracted from each of the 30.72 MHz bandwidth maps. The sources were sorted by their detection signal-to-noise level and, for each of the three maps, were fitted in descending order. For each source, the position and shape (axial ratio and position angle) parameters of the Gaussian fitting function were held fixed to the values determined in the full-band map extraction, while the peak value, background level, and a scaling factor for the widths of both the major and minor axes of the Gaussian were allowed to vary. This procedure was performed for all sources. When the fit successfully converged, the best-fit model was subtracted from the sub-band map. A total of 908 sources were extracted in the Hydra A field and 1100 sources were extracted from the EoR2 field.

6.7. Astrometric Corrections and Flux Calibration

We compared the positions and relative fluxes of the sources identified in the full-band maps with the positions and fluxes of possible counterparts in other catalogs. These comparisons formed the basis for astrometric corrections, and for the determination of the overall MWA flux scale. Counterparts to MWA-32T sources were identified at 408 MHz by locating sources in the MRC which were within 15′ of an MWA source. Although we expect our astrometric accuracy to be much better than 15′, this value was chosen to be comparable to the size of the MWA-32T synthesized beam major-axis FWHM response, viz., 13′ for the Hydra A field and 14′ for the EoR2 field, and to allow for some degree of systematic error in the MWA source positions. To avoid possible blending issues, we only considered an identification to be secure when there was precisely one source in the MRC within 30′ of the (pre-adjustment) MWA source position. A total of 419 sources were matched uniquely to the MRC in the Hydra A field and 520 sources were matched in the EoR2 field.

An astrometric correction was then calculated by allowing for a linear transformation of the MWA source coordinates in order to minimize the positional differences between corresponding MWA and MRC sources. The transformation permits offsets in both right ascension and declination as well as rotation and shear with respect to the field center. Optimal transformation parameters were determined by performing weighted least-squares fits. The results from initial fits indicated that there were errors in the (Earth-referenced) coordinates of the MWA tiles and in the conversion of coordinates in the maps from the epoch of observation frame to the J2000 frame. These errors were then corrected. The final fits were found to be consistent solely with offsets of the MWA source coordinates, with no shear or rotational effects. We therefore applied offsets of $\Delta\alpha = -0.'6$ and $\Delta\delta = 1.'6$ to the positions of the sources in the Hydra A field, and of $\Delta\alpha = 2.'2$ and $\Delta\delta = 1.'9$ to those in the EoR2 field. We believe that the coordinate offsets are likely due to a combination of the effects of structure in Hydra A and to ionospheric refraction. Figure 2 shows the post-offset-correction differences in position between corresponding MWA and MRC sources in the EoR2 field. Histograms of residual positional differences from both the Hydra A and EoR2 fields are plotted in Figure 3. For this figure the difference for each source is normalized by the expected error based on the S/N for the intensity and the 32T synthesized beamwidth (with the assumption of a circular source; see Condon 1997). The residual position differences are generally consistent with those expected, even though there are a small number of large position differences.

A final flux scale was set for each map using the MWA sources which had counterparts in both the MRC and Culgoora source lists. Only sources in the MWA catalog above a detection S/N threshold of 5 were used. Hydra A was excluded for reasons discussed in Section 7.1. A prediction for each source was obtained by fitting a power-law spectrum to the 408 MHz MRC flux and the 80 MHz and 160 MHz Culgoora fluxes. Under these criteria, measurements in all three bands were found for a total of 64 uniquely matching sources in the Hydra A field and 81 uniquely matching sources in the EoR2 field. Using these flux

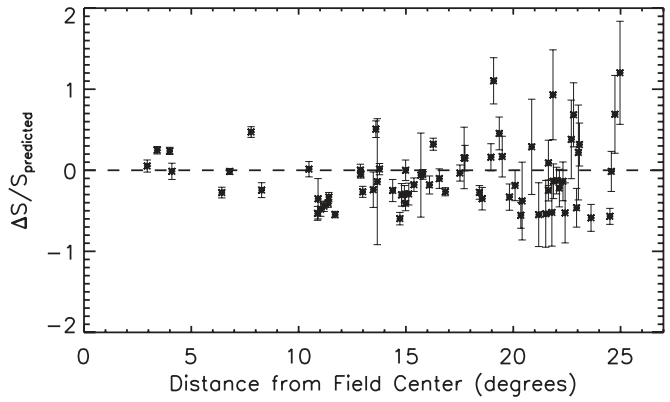

Figure 4. Fractional differences between predicted and measured fluxes for the EoR2 field at 154.24 MHz (described in Section 6.7), where ΔS is defined as the MWA-32T measured flux minus the flux predicted from fitting MRC and Culgoora measurements. The error bars are derived from combining the rms noise in the MWA map at the source position in quadrature with the flux prediction uncertainty. The differences are displayed as a function of distance from the field center, in order to assess the presence of any radial biases in the MWA flux measurements. No significant bias was found out to large distances from the field center.

predictions, a flux scale correction was calculated of the form

$$S_{\rm calibrated} = C_\nu \times S_{\rm uncalibrated}. \quad (8)$$

These calibration terms were calculated independently for each of the three sub-band maps as well as for each averaged map for each field. For the Hydra A field, the calculation yielded $C_\nu = 1.26$ for the full-band average map, 1.17 for the 123.52 MHz map, 1.20 for the 154.24 MHz map, and 1.18 for the 184.96 MHz map, and for the EoR2 field, the calculation yielded $C_\nu = 1.24$ for the full-band average map, 1.19 for the 123.52 MHz map, 1.23 for the 154.24 MHz map, and 1.17 for the 184.96 MHz map. The residuals after applying these flux scale corrections were analyzed to determine if additional biases were present as a function of position in the image (biases would potentially be seen, e.g., if the assumed primary beam model was incorrect). An example of these plots is shown in Figure 4, which shows no evidence for a radially increasing flux bias.

The magnitude of the post-correction residual differences between the MWA measurements and the predicted fluxes for calibration sources are still larger on average than expected under the assumption that the uncertainty in each MWA-32T flux measurement is due to the rms map noise at the source location, and that the uncertainty in the predicted flux of each source is propagated for the power-law fitting procedure. This excess in the differences could be due to errors in the spectral model for the calibration sources, temporal variability of the sources, or to as yet unidentified errors. Since this is the first work based on MWA-32T data to report the fluxes of a large number of sources, we make the conservative assumption that these excessively large residuals are due solely to errors in the MWA-32T flux measurements. We assume that the flux uncertainties follow a Gaussian distribution which includes the effects of the rms map noise added in quadrature with an additional component proportional to the measured flux of the source:

$$\sigma^2_{\rm MWA} = \beta^2 S^2_{\rm MWA} + \sigma^2_{\rm Map}, \quad (9)$$

where $\sigma_{\rm MWA}$ is the 1σ flux uncertainty for a particular source, β is the fractional flux uncertainty, $S_{\rm MWA}$ is the measured source flux, and $\sigma_{\rm Map}$ is the rms map noise at the position of the source.

We evaluated the standard deviation, σ_D, of the fractional flux difference, D, where D is calculated as

$$D = \frac{S_{\rm MWA} - S_{\rm Predicted}}{S_{\rm Predicted}}. \quad (10)$$

We then solved for the fractional uncertainty in the MWA measurements which would be needed to account for the magnitude of the measured value of σ_D:

$$\beta^2 = \sigma_D^2 \left(\frac{S_{\rm Predicted}}{S_{\rm MWA}}\right)^2 - \left(\frac{\sigma_{\rm Predicted}}{S_{\rm Predicted}}\right)^2 - \left(\frac{\sigma_{\rm Map}}{S_{\rm MWA}}\right)^2. \quad (11)$$

We calculated the average value of β separately for each field. For the higher frequency maps, we found that the values of β were much larger far from the field center where the primary beam approaches the first null; for these maps the sources were separated into inner and outer region sets using a cutoff of 18°, and β was calculated separately for each region. Using these results, we assign fractional flux uncertainties of 30% for all sources in the full-band average maps, 35% for all sources in the 123.52 MHz maps, 35% for sources in the inner region of the 154.24 MHz maps, 60% for sources in the outer region of the 154.24 MHz maps, 35% for sources in the inner region of the 184.96 MHz maps, and 80% for sources in the outer region of the 184.96 MHz maps. These fractional uncertainty values are applied to all sources in the catalog by adding them in quadrature to the map rms values as described in Equation (9).

7. RESULTS

7.1. Radio Maps and Source Catalog

The full-band average maps of the Hydra A and EoR2 fields are displayed in Figures 5 and 6. These images overlap partially. Together, they cover ~2700 deg^2. The synthesized beam for the Hydra A field has a major-axis width of 19′ in the 124.52 MHz map, 14′ in the 154.24 MHz map, 12′ in the 184.96 MHz map, and 13′ in the full-band average map. For the EoR2 field, the major-axis beam widths are 18′ in the 124.52 MHz map, 16′ in the 154.24 MHz map, 13′ in the 184.96 MHz map, and 14′ in the full-band average map.

The bright radio galaxy Hydra A is the dominant source in these maps. The flux of the source is measured to be 710 ± 210 Jy in the full-band average map of the Hydra A field, and 550 ± 170 Jy in the full-band average map of the EoR2 field. These measurements of Hydra A are significantly brighter than expected based on previous measurements: the Culgoora 160 MHz measurements give a flux of 243 Jy, and a prediction based off of the Culgoora and MRC measurements (as described in Section 6.7) gives a flux of 284 Jy. Using the VLA, Kassim et al. (2007) find an integrated flux density of 644.2 Jy for Hydra A at 74 MHz, which, when scaled to 154.24 MHz using a spectral index of $\alpha \sim -0.8$, is consistent with the prediction from Culgoora and MRC measurements and inconsistent with the MWA results. Although Hydra A is slightly extended in the MWA-32T maps, the structures seen in the previous low-frequency maps of Hydra A presented by Lane et al. (2004) are below the scale of the MWA synthesized beam. We note that the MWA-32T array has a significantly more compact uv distribution than the VLA, Molonglo, or Culgoora telescopes. A flux from Hydra A above what is expected from the Culgoora measurements is also noted in measurements

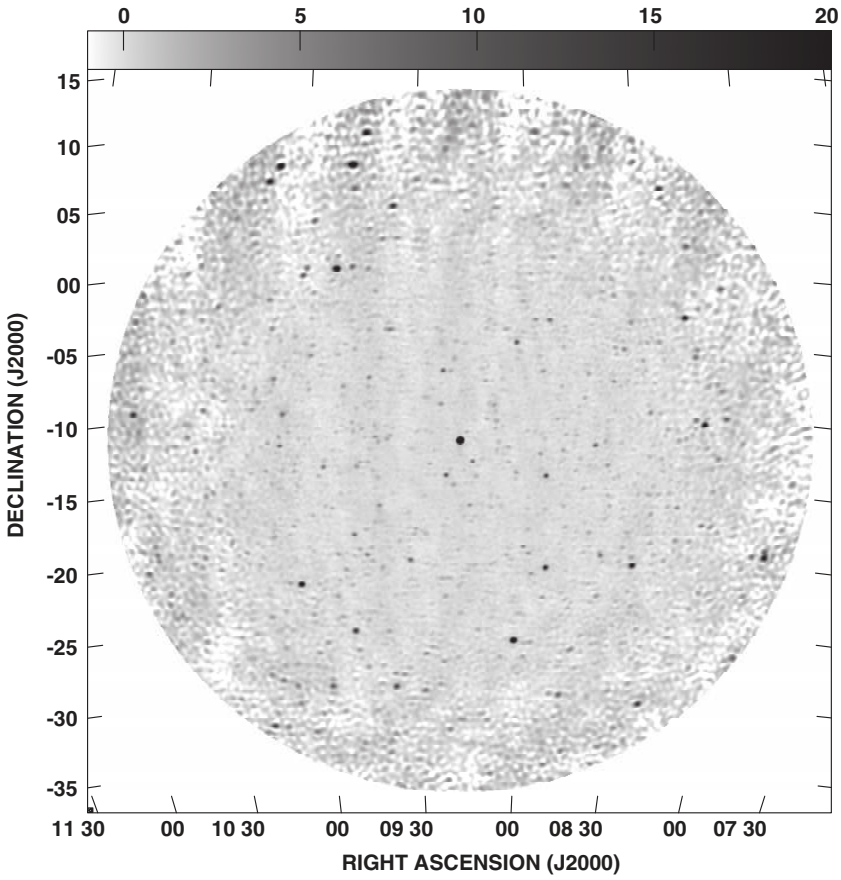

Figure 5. Full bandwidth synthesis map of the Hydra A field, with a 50° diameter. This map was produced using the pipeline described in Section 6, and served as a basis for source identification in this field.

with the PAPER array (D. C. Jacobs 2011, private communication), which has a similar baseline distribution to that of the MWA-32T. Consequently we did not include Hydra A in the final flux scale calibration procedure described in Section 6.7. Resolving this flux discrepancy remains a major outstanding issue.

The behavior of the fitted rms noise in these images is illustrated in Figure 7, which shows annular averages as a function of distance from the field center. We can estimate a lower limit to the rms noise in each map by calculating the classical source confusion limit. Note that this differs from the sidelobe confusion limit; see, e.g., Condon (1974) for a rigorous discussion of classical source confusion in radio telescopes. Di Matteo et al. (2002) present a model of the radio source counts derived from the 6C (Hales et al. 1988) catalog at 150 MHz. Their expression takes the form of a broken power law:[24]

$$\frac{dn}{dS} = \begin{cases} 4000 \left(\frac{S}{1\,\mathrm{Jy}}\right)^{-2.51} \text{ sources Jy}^{-1}\,\text{sr}^{-1}, & S > S_0 \\ 4000 \left(\frac{S_0}{1\,\mathrm{Jy}}\right)^{-0.76} \left(\frac{S}{1\,\mathrm{Jy}}\right)^{-1.75} \text{ sources Jy}^{-1}\,\text{sr}^{-1}, & S < S_0, \end{cases} \quad (12)$$

where $S_0 = 0.88$ Jy. Integration of this expression gives the source density in each beam above a minimum flux value, $S_{\min}$:

$$\rho_S = \frac{\pi\theta^2}{4\ln 2} \int_{S_{\min}}^{\infty} \frac{dn}{dS} dS \text{ sources beam}^{-1}, \quad (13)$$

where ρ_S is the source density in units of sources per beam and θ is the FWHM synthesized beam size. The source confusion limit then corresponds to the flux, $S_{\min}$, for which the source density approaches one source per synthesized beam area (typically maps are considered to be source confusion limited when they have a source density of greater than 1 source per 10 synthesized beams). The average rms noise (Figure 7) reaches a minimum value of ~160 mJy for the full-band average map of the EoR2 field. Using the corresponding flux threshold for an unresolved source of $S_{\min} = 160$ mJy in combination with the EoR2 full-band map synthesized beam area gives $\rho_S \sim 0.30$ sources per synthesized beam, or, in other words, one source of at least 160 mJy in roughly every three synthesized beams. Estimates for the other average and sub-band maps give expected source densities of one source per every three to six synthesized beams. Thus, source confusion is likely the limiting source of noise in the central region of these maps. This explains the relatively flat nature of the central noise floor seen in Figure 7. Near the edges of the images, not far from the first null of the primary beam, we expect the noise to be dominated by receiver noise, and to scale with the inverse of the primary beam power pattern. This is also seen in Figure 7 (the frequency dependence of the noise curves illustrates the frequency dependence of the primary beam).

[24] The notation of Di Matteo et al. (2002) is ambiguous, and is interpreted differently by several authors. We note that Lidz et al. (2008) quote a modified form of the expression, which affects the normalization of the power law. Although the Lidz et al. (2008) expression fits the 6C source counts slightly better at high flux values, the formulation presented in this paper fits the data better throughout the entire flux range. The expression from Di Matteo et al. (2002) has been corrected with an additional minus sign to make it continuous across the transition at $S = S_0$.

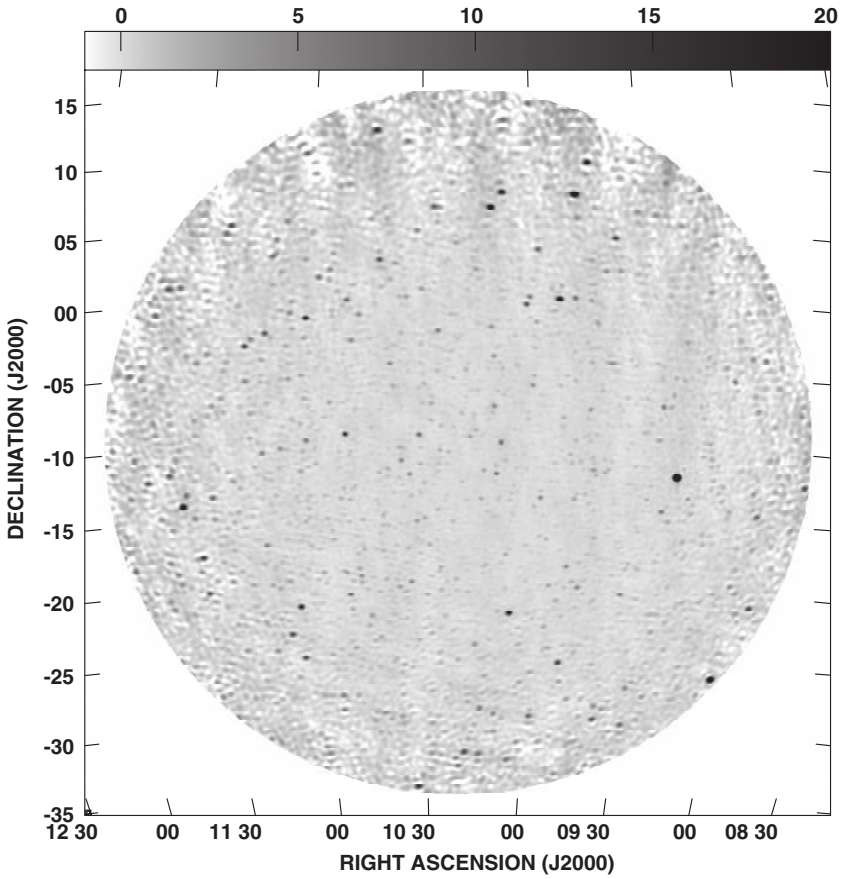

Figure 6. Full bandwidth synthesis maps of the EoR2 field, with a 50° diameter. This map was produced using the pipeline described in Section 6, and served as a basis for source identification in this field.

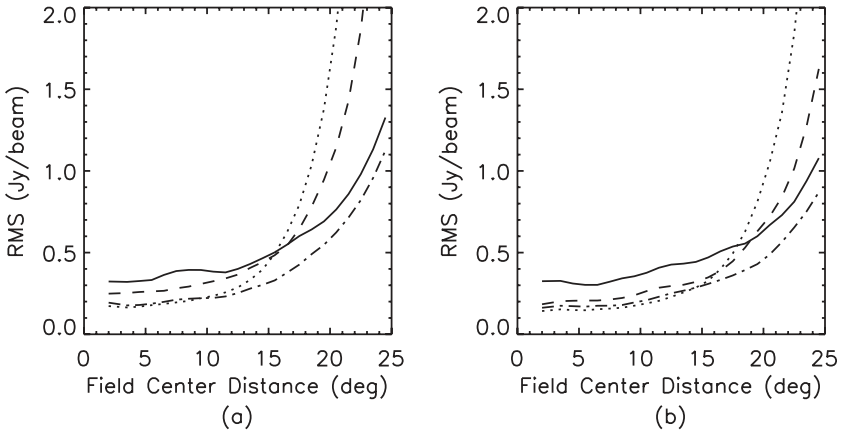

Figure 7. Radial dependence of the calculated rms noise in the Hydra A (a) and EoR2 (b) field images. The rms is plotted for the three sub-band maps, with central frequencies of 123.52 MHz (solid lines), 154.24 MHz (dashed lines), and 184.96 MHz (dotted line) as well as for the full-band-averaged maps (dot-dashed lines). The values shown are the medians of 1° wide radial annuli. The points are connected with lines for clarity. The frequency-dependent primary beam shape is evident from the increasing rms at large distance from the field center, and the confusion-limited nature of the maps is illustrated by the flat rms profile near the center of the field. The minimum rms approaches a value of ∼130 mJy beam^{-1}.

A catalog was constructed from the 2008 detections at a detection S/N threshold $\geqslant$3 of potential sources in the EoR2 and Hydra A fields. In the cases where there were detections at corresponding celestial positions in the two fields, the measurement where the source was closer to the observation field center was retained, resulting in a list of 1526 unique source detections. The quality of this source list is assessed in Sections 7.2 and 7.3 as a function of the detection S/N level. The 655 sources detected at an S/N level $\geqslant$5 in the detection images are reported in Table 2. The 871 sources with $3 \leqslant$ S/N < 5 are considered to be less reliable detections. A list of these candidate detections can be obtained by contacting the authors.

7.2. Reliability of the Source List

The reliability of the identified sources was evaluated through comparison with the flux-limited sample from MRC, VLSS, and maps from TGSS. The MRC source list has a well-defined completeness flux limit and covers our entire field; however it gives fluxes at a different frequency (408 MHz) and does not go quite as deep as our survey. VLSS covers a portion of our fields at

Table 2
Detected Sources in the Hydra A and EOR 2 Fields

Name	R.A.	Decl.	S_{avg}	$S_{123.52}$	$S_{154.24}$	$S_{184.96}$	Field	r_{FC}	Detection S/N Level
J0747−1854	$07^h47^m05^s$	$-18°54'12''$	8.8 ± 2.8	10.1 ± 3.7	9.2 ± 6.0	8.9 ± 8.5	HydA	22.°9	8.6
J0747−1919	$07^h47^m27^s$	$-19°19'33''$	22.2 ± 6.7	25.2 ± 8.9	23.8 ± 14.5	15.1 ± 13.0	HydA	23.°0	22.4
J0751−1919	$07^h51^m20^s$	$-19°19'30''$	7.1 ± 2.2	8.1 ± 3.0	8.5 ± 5.3	4.7 ± 5.1	HydA	22.°1	8.7
J0752−2204	$07^h52^m30^s$	$-22°04'38''$	4.4 ± 1.5	4.7 ± 1.8	7.1 ± 4.5	14.4 ± 12.1	HydA	22.°7	5.6
J0752−2627	$07^h52^m30^s$	$-26°27'43''$	8.4 ± 2.7	9.8 ± 3.7	3.6 ± 3.1	...	HydA	24.°7	7.0
J0757−1137	$07^h57^m10^s$	$-11°37'10''$	3.9 ± 1.3	4.7 ± 1.8	5.1 ± 3.3	2.5 ± 2.5	HydA	19.°8	6.0
J0802−0915	$08^h02^m18^s$	$-09°15'32''$	3.4 ± 1.2	5.8 ± 2.2	2.1 ± 1.5	1.9 ± 1.8	HydA	18.°8	5.0
J0802−0958	$08^h02^m34^s$	$-09°58'55''$	8.9 ± 2.8	12.4 ± 4.4	6.0 ± 3.7	9.1 ± 7.3	HydA	18.°6	12.6
J0803−0804	$08^h03^m60^s$	$-08°04'48''$	4.5 ± 1.4	6.5 ± 2.4	2.4 ± 1.6	6.7 ± 5.4	HydA	18.°7	7.0
J0804−1244	$08^h04^m17^s$	$-12°44'32''$	4.6 ± 1.5	4.8 ± 1.8	5.2 ± 3.2	4.5 ± 3.7	HydA	18.°0	9.3
J0804−1726	$08^h04^m42^s$	$-17°26'41''$	4.9 ± 1.5	5.8 ± 2.1	4.5 ± 2.8	3.1 ± 2.6	HydA	18.°5	9.1
J0804−1502	$08^h04^m53^s$	$-15°02'54''$	2.8 ± 0.9	2.2 ± 1.0	4.6 ± 2.9	1.0 ± 1.1	HydA	18.°0	6.4
J0805−0100	$08^h05^m30^s$	$-01°00'12''$	9.4 ± 2.9	10.8 ± 3.9	8.3 ± 5.2	6.4 ± 5.4	HydA	21.°1	10.4
J0805−0739	$08^h05^m40^s$	$-07°39'22''$	3.5 ± 1.2	4.4 ± 1.7	3.7 ± 2.4	1.9 ± 1.9	HydA	18.°4	5.5
J0806−2204	$08^h06^m26^s$	$-22°04'43''$	3.7 ± 1.2	4.2 ± 1.6	3.8 ± 2.4	3.6 ± 3.1	HydA	19.°8	6.2

Notes. The flux of each source detected in the MWA full-band-averaged maps is presented along with the flux measured in each 30.72 MHz sub-band. Duplicate sources in the region of overlap of the two fields are not listed. Missing data indicate that the automatic source measurement algorithm failed to converge in a flux fit for that source in the sub-band map. The field from which each source measurement comes from is listed, along with the distance of the source from the center of the field (r_{FC}). We expect systematic errors to be larger for sources far from the field center. The "Detection S/N Level" indicates the signal-to-noise ratio at which the source was detected in the full-band-averaged map. Section 7.2 discusses the reliability of the catalog at different detection S/N levels. This list includes sources identified above a detection S/N threshold of 5. The full source list of all sources above a detection S/N threshold of 3 is available from the authors.

(This table is available in its entirety in a machine-readable form in the online journal. A portion is shown here for guidance regarding its form and content.)

a lower frequency than MWA (74 MHz), and provides a useful complementary assessment. The TGSS maps are at the same frequency as the MWA observations (150 MHz), but the maps which have been released to date only cover a small fraction of our fields and are based on a significantly different sampling of the visibility function due to the different array baselines.

In order to assess the MWA-32T catalog reliability, we first evaluate the detectability of an MWA source in the external comparison survey. The MWA full-band average flux is extrapolated to the relevant frequency using a spectral index of $\alpha = -0.8$, and the extrapolated value is then compared to the parameters of the comparison map or catalog to evaluate whether it meets the detection criteria for that survey. If the source is deemed detectable, then we search for a companion source in that catalog or map to see if the source was actually detected by the other survey. Under the assumption that the other surveys are complete, this allows us to assess how many spurious sources are present in the MWA catalog. We define the reliability as

$$R = \frac{N_{\rm detected}/N_{\rm detectable} - f}{1 - f}, \quad (14)$$

where R is the fraction of MWA sources we believe to be reliable, $N_{\rm detectable}$ is the number of MWA sources which we believe should have been detectable in the comparison survey, $N_{\rm detected}$ is the number of detectable MWA sources for which we found counterparts in the other survey, and f is the false source coincidence fraction. We determine f by calculating the source density of the comparison survey in the MWA fields, and use our counterpart matching criteria to estimate the probability that a randomly chosen sky location will lead to an association with a source in the comparison survey. This analysis was performed for different MWA source detection thresholds.

For the reliability comparison with the MRC, we used the completeness limit of 1 Jy (Large et al. 1981) to assess the detectability of the extrapolated MWA source fluxes. An MRC counterpart is associated with the MWA source if it is within 10′ of the MWA source position. Based off of the counterpart search radius and source densities in the MRC field, we estimate a false coincidence chance of 4%. A fixed flux completeness limit is not given for the VLSS, however Cohen et al. (2007) note that for a typical VLSS rms of 0.1 Jy beam^{-1}, the 50% point-source detection limit is approximately 0.7 Jy. We then assume that the VLSS is complete down to a flux level of 1 Jy, and we again use a 10′ source association radius in the reliability calculation. At the present time, the VLSS catalog does not cover the entire combined EoR2 and Hydra A region that we have surveyed. To ensure we are only including sources in the VLSS survey area, we only analyzed MWA sources above a declination of $\delta = -25°$. We estimate a false coincidence chance of 18% for the VLSS matching.

The cumulative and differential catalog reliabilities are listed as functions of the MWA detection level in Tables 3 and 4. We view these reliability estimates as lower limits, particularly at the lower flux levels, because our assessments of comparison survey detectability do not take into account errors in the source flux extrapolation or source time variability. MWA sources which are erroneously calculated as detectable will not, in general, lead to detections of counterparts in the comparison catalog, whereas sources erroneously calculated as undetectable will be omitted from the analysis and, therefore, will not be included in the calculation of the reliability ratio. These catalog comparisons imply a reliability of $\gtrsim$99% for sources detected above a detection S/N of 5.

For the reliability comparison using TGSS, we used the maps from TGSS Data Release 2 available at the time of our analysis. Although the baseline distribution of GMRT is substantially different from that of MWA-32T, GMRT has a compact central array consisting of 14 antennas within an area of radius 500 m (Swarup et al. 1991) that leads to substantial overlap with MWA-32T regarding the region of the uv plane that was sampled. Twenty-seven TGSS fields overlapped the EoR2 field; none overlapped the Hydra A field. We modeled the effects of source

Table 3
Cumulative Source Reliability

Detection S/N	MRC Reliability		VLSS Reliability		TGSS Reliability	
Threshold	$N_{\rm detected}/N_{\rm detectable}$	R	$N_{\rm detected}/N_{\rm detectable}$	R	$N_{\rm detected}/N_{\rm detectable}$	R
>3	488/589	82%	1215/1312	91%	183/197	93%
>4	421/444	95%	826/839	98%	132/133	99%
>5	349/357	98%	575/579	99%	85/85	100%
>7	257/259	99%	325/326	100%	49/49	100%
>10	167/167	100%	173/173	100%	26/26	100%

Notes. The reliability is assessed by comparing the MWA source list with the MRC catalog, VLSS catalog, and convolved TGSS maps as described in Section 7.2. The MRC and VLSS comparisons are made by extrapolating the MWA source flux to 408 MHz and 74 MHz, respectively, assuming a spectral index of $\alpha = -0.8$, to assess the detectability of the MWA source in the catalogs. The TGSS results are based on using sources in convolved TGSS maps above 4σ significance. The reliability percentages, R, have been corrected for false positives.

Table 4
Differential Source Reliability

Detection S/N	MRC Diff. Reliability		VLSS Diff. Reliability		TGSS Diff. Reliability	
Threshold (DT)	$N_{\rm detected}/N_{\rm detectable}$	R	$N_{\rm detected}/N_{\rm detectable}$	R	$N_{\rm detected}/N_{\rm detectable}$	R
$3 < {\rm DT} \leqslant 4$	67/145	44%	389/473	78%	51/64	80%
$4 < {\rm DT} \leqslant 5$	72/87	82%	251/260	96%	47/48	98%
$5 < {\rm DT} \leqslant 6$	43/48	89%	142/144	98%	20/20	100%
$6 < {\rm DT} \leqslant 7$	49/50	98%	108/109	99%	16/16	100%
$7 < {\rm DT} \leqslant 8$	33/34	97%	68/69	98%	15/15	100%
$8 < {\rm DT} \leqslant 9$	31/32	97%	44/44	100%	7/7	100%
$9 < {\rm DT} \leqslant 10$	26/26	100%	40/40	100%	1/1	100%

Notes. The reliability is assessed by comparing the MWA source list with the MRC catalog, VLSS catalog, and convolved TGSS maps for various ranges of detection S/N threshold (DT) as discussed in Section 7.2. The MRC and VLSS comparisons are made by extrapolating the MWA source flux to 408 MHz and 74 MHz, respectively, assuming a spectral index of $\alpha = -0.8$, to assess the detectability of the MWA source in the catalogs. The TGSS results are based on using sources in convolved TGSS maps above 4σ significance. The reliability percentages, R, have been corrected for false positives.

blending by the large MWA beam by convolving the CLEANed and restored TGSS maps to a Gaussian FWHM resolution of 12′. Care was taken in the convolution to preserve the flux density scale. The resulting convolved images have typical rms surface brightness fluctuations of ∼0.4 Jy beam^{-1} in regions free of sources. Sources in these maps were identified by taking all pixels above 4σ and associating a source with each island of bright pixels. The resulting TGSS source catalog was compared to those sources in the MWA list with flux density greater than the 4σ level in the TGSS field, and thus expected to be detected in the TGSS field. Pairs of sources in the two catalogs coincident within 10′ were recorded as sources detected in both surveys. MWA sources without a TGSS counterpart were counted as non-detections. Reliability values are presented in Tables 3 and 4. These values are ratios for each MWA detection S/N bin of the number of TGSS detections to the number of MWA sources expected to be detected in the TGSS field, and are, of course, a function of the threshold chosen in the TGSS maps. As an example of the TGSS comparison we present Figure 8, which plots the positions of MWA and MRC sources on a grayscale image of a convolved TGSS field. It is important to note that these reliability estimates solely test for the presence of a source coincident with the reported position, and do not speak to the fidelity of the fluxes of these sources or whether the MWA sources are due to single objects or blends of multiple fainter objects.

7.3. Completeness of the Source Catalog

We used the Culgoora source list to assess the completeness of the MWA catalog presented in this paper. We chose the Culgoora list because it includes observations done at 160 MHz, a frequency not far from the midpoint of the MWA band and because its synthesized beam is similar in size to that of MWA-32T. For each Culgoora source within a field observed by MWA we used the position-dependent rms noise in the MWA full-band-averaged maps to evaluate its detectability in the MWA map. Culgoora sources which should be detectable above a specified S/N level in the MWA images were then checked for a matching source within 10′ in the MWA catalog. Since we used the Culgoora source list to assess the completeness, the results are only valid down to a level comparable to the lowest Culgoora fluxes of ∼1.2 Jy. The completeness ratio was calculated similarly to the reliability described in Section 7.2:

$$C = \frac{N_{\rm detected}/N_{\rm detectable} - f}{1 - f}, \quad (15)$$

where C is the completeness percentage, $N_{\rm detectable}$ is the number of Culgoora sources which we believe should have been detectable in the MWA source list, $N_{\rm detected}$ is the number of detectable Culgoora sources for which we found counterparts in the MWA list, and f is the false source coincidence fraction calculated from the MWA catalog source density using the 10′ source matching criteria. The results are presented in Table 5.

The completeness was analyzed separately for sources within inner and outer regions separated by a circle of radius $r = 18^\circ$ around the field center. All Culgoora sources within the inner region which did not have a corresponding detection in the MWA source list were inspected and found to coincide with a local maximum in the map, implying that the completeness is limited by the robustness of the source extraction algorithm and the flux calibration rather than the intrinsic map quality. It is important to note that because the MWA maps have a sensitivity

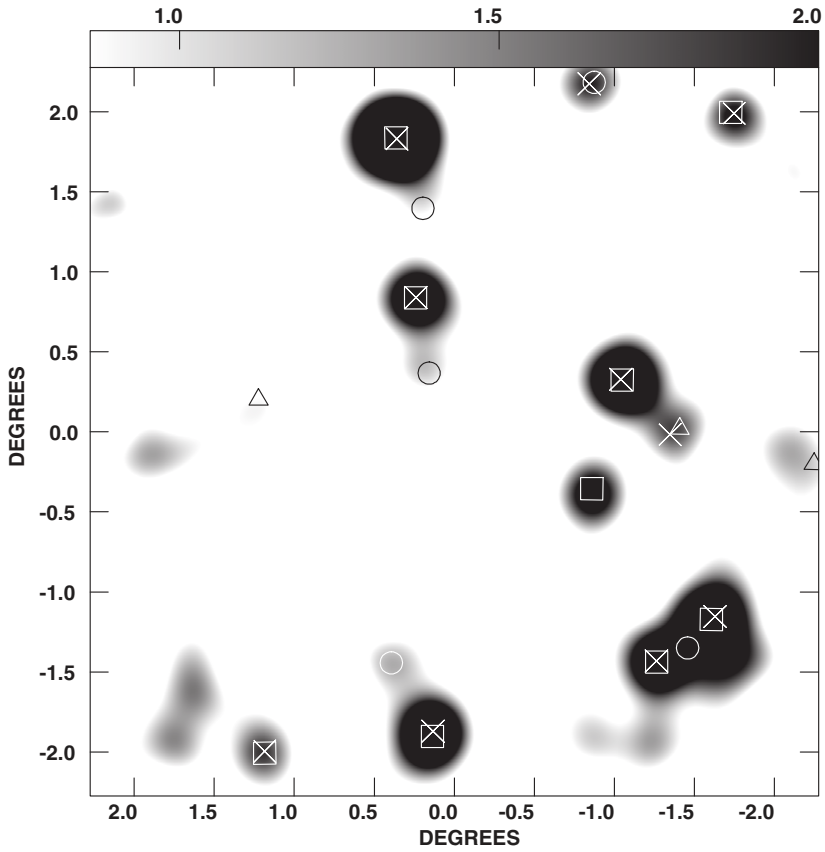

Figure 8. Grayscale image of a TGSS field (field R33D18), with positions of MWA and MRC sources overlaid. Only pixels with S/N > 4 are plotted, and the mapping of pixels to gray scale is shown by the scale in Jy beam^{-1} at the top of the image. Positions of MWA sources with Detection Threshold >5 are plotted with a square, of MWA sources with 4 < Detection Threshold ⩽ 5 are plotted with a circle, of MWA source with 3 < Detection Threshold ⩽4 with a triangle, and of MRC sources with an X. All MWA and MRC sources in this field have a counterpart in the TGSS image. There are five sources in the field that are detected in the MWA and TGSS surveys, but not in the MRC.

Table 5
Source List Completeness

Field	$r < 18°$		$r > 18°$	
Name	$N_{\rm detected}/N_{\rm detectable}$	Completeness	$N_{\rm detected}/N_{\rm detectable}$	Completeness
Detection S/N level ⩾5				
Hydra A	56/63	89%	36/44	82%
EoR2	72/77	93%	49/58	84%
Detection S/N level ⩾3				
Hydra A	62/63	98%	52/67	77%
EoR2	75/77	97%	61/66	92%

Notes. The completeness as assessed by a comparison with the Culgoora source list (Slee 1995), as described in Section 7.3. The minimum source flux in the Culgoora list is ∼1.2 Jy, so these results are only valid for sources brighter than this level. We view these completeness estimates as a lower limit on the catalog completeness—source variability or flux errors in the Culgoora measurement will decrease the calculated completeness ratio. Due to the varying sensitivity across the MWA field, the completeness is calculated relative to the local noise in the MWA source detection map, rather than an absolute flux level. The completeness percentages have been corrected for false positives as described in Section 7.3. Analyzing the source counts in the field (see Section 7.4) indicates that the source list is complete above ∼2 Jy.

that varies strongly across the field, this completeness value does not specify a flux limit to the catalog, but rather assesses the efficacy of the source extraction. As with the above reliability estimate, variability and incompleteness act to make this a lower limit on the true completeness.

7.4. Source Counts and Correlation Function

Radio source counts provide another useful diagnostic test to assess the quality of the catalog and consistency with previous works. As discussed in Section 7.1, Di Matteo et al. (2002) fit the 151 MHz 6C survey results of Hales et al. (1988) to obtain a power-law model for radio source counts. The fit is valid up to ∼10 Jy, but the actual 6C counts fall somewhat below the fit at the high end of the range. Using the MWA-32T catalog generated from the EoR2 field, we calculate the differential source counts, using the noise map of the field to correct for the effects of sensitivity variations on the effective survey area for different flux values (i.e., bright sources can be detected over a

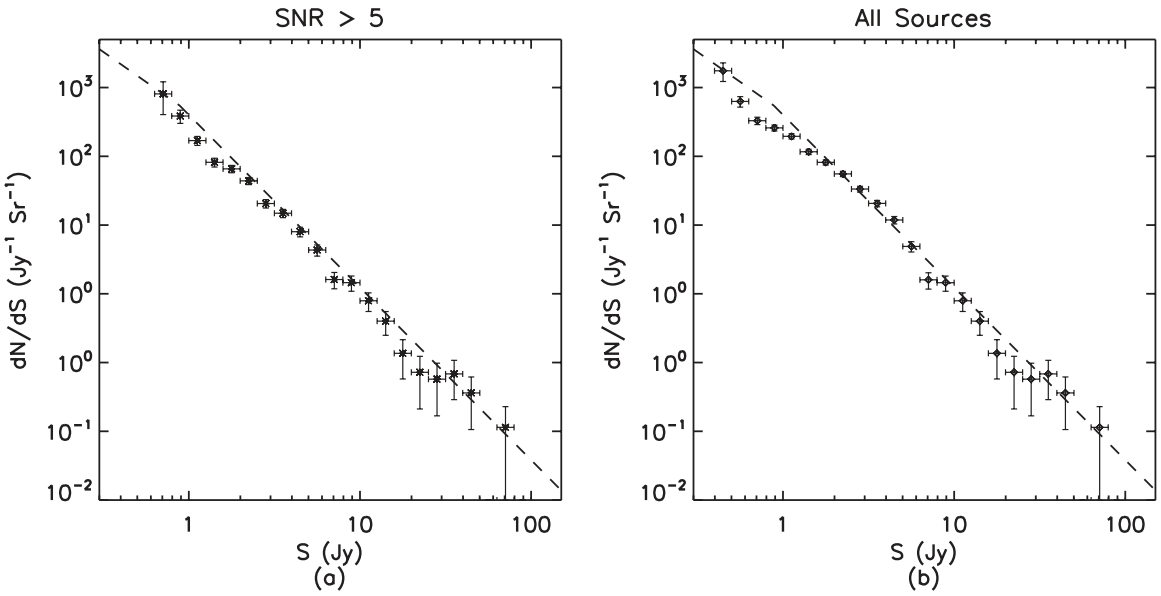

Figure 9. Differential source counts histograms from the MWA EoR2 field, calculated using both the high reliability catalog (a) and the full list of source candidates (b). The noise maps were used to correct for the effective area surveyed in each bin. Poisson error bars are assigned based on the number of counts in each bin. No Eddington bias correction is applied. The source counts model from Di Matteo et al. (2002) is shown for reference with a dashed line. We believe that the deviations from the Di Matteo et al. (2002) model below $S \sim 3$ Jy are not due to an intrinsic change in the source counts distribution at this scale, but are instead due to incompleteness of the source catalog in this flux range.

larger area than faint sources). No Eddington bias correction is applied (to correct for the artificial enhancement of faint sources due to noise in the map) and the error bars are calculated from the square root of the number of counts in each bin. These source counts are shown in Figure 9, along with the expected source counts from integrating the Di Matteo et al. (2002) model. We note that more sophisticated models of 150 MHz source counts models have been described by, e.g., Wilman et al. (2008) and Jackson (2005). These models have different behavior at the sub-Jansky flux levels that have been probed by high resolution, deep, narrower field-of-view studies such as those described in Intema et al. (2011) and Ishwara-Chandra et al. (2010). We compare our results with the Di Matteo et al. (2002) source counts model because it is commonly used as a basis for studies of EoR foregrounds and sensitivities.

The results from the catalog presented in this work agree with the Di Matteo et al. (2002) model above flux levels of ∼2 Jy. Below this level, the MWA-32T source counts diverge from the model, likely because of the incompleteness of the MWA source extraction for low flux sources. A power-law fit to the EoR2 field source counts above 2 Jy yields $dn/dS = (3500 \pm 500)(S/1\,\mathrm{Jy})^{-2.59\pm0.09}$ sources Jy^{-1} sr^{-1} for sources with a detection S/N greater than 5. Fitting for a power law to the full list of sources in the field down to a detection S/N of 3 yields $dn/dS = (5700 \pm 700)(S/1\,\mathrm{Jy})^{-2.76\pm0.08}$ sources Jy^{-1} sr^{-1}.

As an additional test for systematic effects, we have constructed the angular two-point correlation function, $w(\theta)$, of the sources in our catalog. This correlation function can show systematic effects that manifest themselves on characteristic angular scales in the catalog—see, e.g., Blake & Wall (2002). We measure $w(\theta)$ using the estimator defined by Hamilton (1993):

$$w(\theta) = \frac{DD(\theta)RR(\theta)}{DR(\theta)} - 1, \quad (16)$$

where $DD(\theta)$ is the measured angular autocorrelation function from the MWA source catalog, $RR(\theta)$ is the autocorrelation function calculated using a simulated "mock" catalog, and $DR(\theta)$ is the cross-correlation between the MWA and the mock catalog. We generate an ensemble of 100 mock catalogs and evaluate the correlation function with each one separately in order to produce a set of normally distributed estimates of $w(\theta)$. Each mock catalog is produced using an approach developed to simulate point sources at cosmic microwave background and far-IR frequencies (Argüeso et al. 2003; González-Nuevo et al. 2005), but tailored specifically for the MWA experiment (A. de Oliveira-Costa et al., in preparation), i.e., we drew sources from the observed MWA-32T source counts distribution described above in accordance with the expected low-frequency source clustering statistics (de Oliveira-Costa & Capodilupo 2010; de Oliveira-Costa & Lazio 2010). On the angular scales probed by this survey, no observable clustering is expected. By constructing the mock catalogs in this manner, and correlating them with the observed distribution, the resulting estimate of $w(\theta)$ identifies any unexpected correlation which may be due to systematic errors in our survey or in our catalog construction procedure. Figure 10 shows our measurement of $w(\theta)$ above a flux limit of $S \approx 3$ Jy (black squares). Distances between the observed and/or simulated sources are measured in bins of ∼1°, which is substantially above the MWA resolution. The mean value of $w(\theta)$ is shown, along with uncertainties derived from calculating the covariance between $w(\theta)$ bins in the mock catalogs. As expected, $w(\theta)$ is consistent with zero, implying that there is no excess correlation in our catalog.

7.5. Comparison with PAPER Results

Comparing the present results from MWA with results from PAPER (Parsons et al. 2010) is a particularly useful exercise, as both arrays are new, broadband, wide field-of-view instruments with similar uv coverage, and both are intended to be used to make EoR power spectrum measurements. We find that 43 of the sources found in the survey (described in Section 2) of Jacobs et al. (2011) are located in our survey region. A search in our MWA-32T catalog reveals unique counterparts within 30′ (the PAPER beam size used by Jacobs et al. 2011 for source

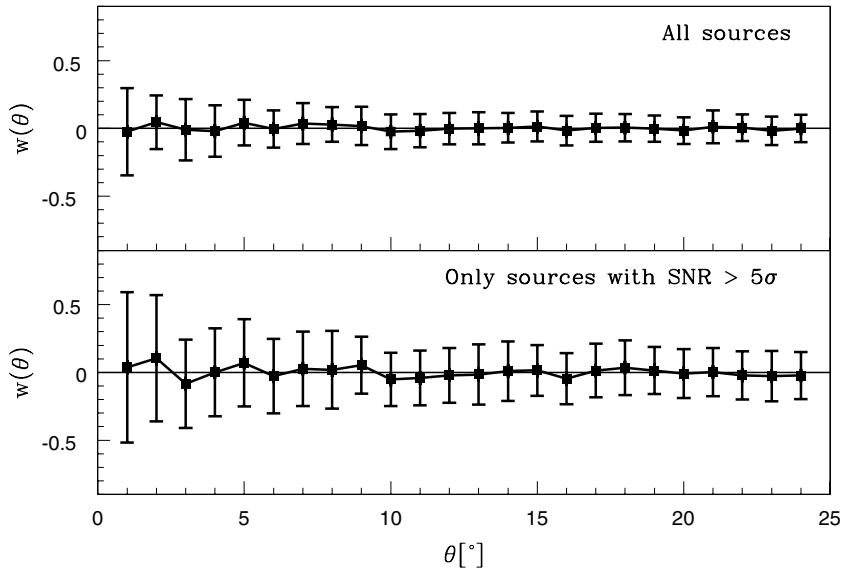

Figure 10. Measured angular correlation function, $w(\theta)$, of the full MWA catalog. The angular correlations are calculated using sources with fluxes above $S \sim 3$ Jy. The top panel shows $w(\theta)$ calculated from all sources in our final catalog, while the bottom panel shows $w(\theta)$ calculated only from sources detected above a detection S/N threshold of 5. As expected, the results are consistent with zero correlation.

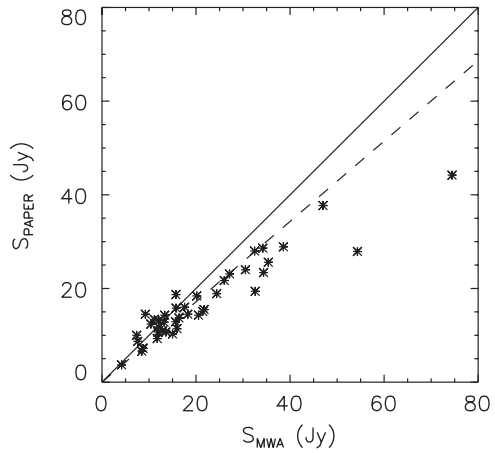

Figure 11. Comparison of the fluxes presented in this work with those from the 145 MHz PAPER source list presented in Jacobs et al. (2011). Error bars have been omitted from the plot for clarity. A total of 43 sources from the PAPER list are within the MWA field. MWA sources, which are within 30′ of a PAPER source are matched. A total of 31 of the PAPER sources had unique counterparts, while 11 PAPER sources matched with multiple MWA sources and 1 PAPER source did not have a detected MWA counterpart (although there is a local maximum in the MWA map at the location of the PAPER source). The MWA fluxes are calculated by summing the flux of all MWA sources which match with a PAPER source, and scaling the flux to a frequency of 145 MHz assuming a spectral index of $\alpha = -0.8$ ($S \propto \nu^{-\alpha}$). The solid line shows the unity flux-ratio locus; the MWA sources are on average 17% brighter than the PAPER sources. This fitted flux-ratio locus is plotted as a dashed line.

association) of the PAPER locations for 31 out of these 43 sources, multiple counterparts in 11 cases, and no counterpart in 1 case. A comparison of the fluxes of sources detected in both the MWA-32T and PAPER catalogs is shown in Figure 11.

The one source with no MWA counterpart is 24° from the center of the MWA Hydra A field, and corresponds to a local maximum in the MWA image; however, it was not detected by the automatic source finding algorithm. For each of the 10 sources with multiple MWA counterparts, an estimate of the blended flux was obtained by summing the flux of all MWA sources within the PAPER beam. Other than Hydra A, all 41 PAPER fluxes are consistent with the MWA blended fluxes (the Hydra A flux reported in the PAPER catalog was corrupted by the filtering used in the PAPER analysis; D. C. Jacobs 2011, private communication). A weighted average of the ratios of the MWA and PAPER source fluxes yields the average ratio $\langle S_{\rm MWA}/S_{\rm PAPER}\rangle = 1.17 \pm 0.10$. However, we note that the PAPER flux scale was set using measurements of two calibration sources from the Culgoora source list, whereas the MWA-32T flux scale was set using a fit to an ensemble of Culgoora and MRC measurements. Slee (1977) note that the Culgoora flux scale may be depressed by 10%, with additional flux uncertainties of between 13% and 39% for individual source measurements. If these Culgoora flux uncertainties are taken into account as potential errors on the PAPER flux scale, then the significance of the difference between the MWA and PAPER flux scales is decreased.

The standard deviation of the MWA to PAPER flux ratios after correcting for the different flux scales is ∼25%. This is smaller than our estimate of the MWA flux uncertainties based on flux predictions from the MRC and Culgoora measurements. This indicates that the flux comparison with the MRC and Culgoora lists may be affected to a considerable extent by radio source variability or other systematic effects.

7.6. Candidate Ultra-steep Spectrum Sources

USS radio sources form a compelling class of candidate high-redshift radio sources (De Breuck et al. 2000, 2002; Di Matteo et al. 2004; Broderick et al. 2007). Low-frequency radio observations are particularly sensitive to these objects (see, e.g., Pedani 2003). We have conducted an analysis of the sources detected in the MWA fields in an attempt to identify additional USS radio sources. A table of candidates is presented in Table 6. We calculated spectral indices by using the PMN 4.85 GHz survey (Griffith & Wright 1993) together with the MWA full-band average flux measurements. We associated MWA sources with PMN counterparts if their positions were coincident within 5′. To avoid source confusion and blending issues, we excluded any MWA sources with more than one PMN counterpart within a 30′ radius. A total of 331 sources were identified for which we could unambiguously identify

Table 6
Ultra-steep Spectrum Source Candidates

Name	R.A.	Decl.	$S_{MWA,avg}$	S_{PMN}	α_{PMN}	S_{MRC}	α_{MRC}	Detection S/N Level
J1009−1207	$10^h09^m19^s$	−12°07′46″	10.69 ± 3.21	0.17 ± 0.01	−1.20 ± 0.09	3.23 ± 0.11	−1.23 ± 0.31	52.5
J1032−3421	$10^h32^m60^s$	−34°21′19″	17.38 ± 5.31	0.27 ± 0.02	−1.21 ± 0.09	5.59 ± 0.25	−1.17 ± 0.32	15.5
J1042+1201	$10^h42^m56^s$	+12°01′30″	15.55 ± 4.80	...	<−1.66 ± 0.09	8.90 ± 0.37	−0.57 ± 0.32	15.1
J1034+1111	$10^h34^m13^s$	+11°11′23″	5.89 ± 1.92	...	<−1.38 ± 0.09	3.80 ± 0.16	−0.45 ± 0.34	8.3
J1000+1400	$10^h00^m16^s$	+14°00′17″	7.54 ± 2.51	...	<−1.45 ± 0.10	3.06 ± 0.10	−0.93 ± 0.34	6.3
J0831−2922	$08^h31^m24^s$	−29°22′26″	3.65 ± 1.24	...	<−1.24 ± 0.10	1.51 ± 0.06	−0.91 ± 0.35	5.7
J1007+1246	$10^h07^m28^s$	+12°46′50″	7.46 ± 2.52	...	<−1.45 ± 0.10	...	...	5.6
J0855+0552	$08^h55^m18^s$	+05°52′50″	4.11 ± 1.40	0.06 ± 0.01	−1.23 ± 0.12	1.62 ± 0.07	−0.96 ± 0.35	5.4
J0834−3443	$08^h34^m29^s$	−34°43′22″	6.14 ± 2.12	...	<−1.40 ± 0.10	...	...	5.0
J0828−3201	$08^h28^m14^s$	−32°01′26″	4.68 ± 1.66	...	<−1.32 ± 0.10	...	...	4.8
J1001+1108	$10^h01^m01^s$	+11°08′19″	3.98 ± 1.37	...	<−1.27 ± 0.10	1.57 ± 0.06	−0.96 ± 0.36	4.6
J0832−3326	$08^h32^m38^s$	−33°26′00″	5.14 ± 1.84	...	<−1.34 ± 0.10	2.30 ± 0.09	−0.83 ± 0.37	4.4
J1008+1201	$10^h08^m11^s$	+12°01′07″	4.48 ± 1.65	...	<−1.30 ± 0.11	...	...	4.2
J1028+1158	$10^h28^m32^s$	+11°58′58″	3.56 ± 1.30	...	<−1.24 ± 0.11	...	...	4.1
J1112+1112	$11^h12^m45^s$	+11°12′45″	4.88 ± 1.92	...	<−1.33 ± 0.11	1.45 ± 0.07	−1.25 ± 0.41	3.8
J1021+1303	$10^h21^m34^s$	+13°03′55″	3.76 ± 1.47	...	<−1.25 ± 0.11	...	...	3.7
J1034+1428	$10^h34^m18^s$	+14°28′48″	4.68 ± 1.85	...	<−1.32 ± 0.11	...	...	3.5
J1104+1103	$11^h04^m21^s$	+11°03′31″	5.35 ± 2.01	...	<−1.36 ± 0.11	...	...	3.4
J0827−3322	$08^h27^m30^s$	−33°22′43″	3.61 ± 1.47	...	<−1.24 ± 0.12	...	...	3.4
J0918+1226	$09^h18^m48^s$	+12°26′31″	5.67 ± 2.34	...	<−1.37 ± 0.12	2.02 ± 0.09	−1.06 ± 0.43	3.3
J1027+1347	$10^h27^m10^s$	+13°47′25″	3.94 ± 1.52	...	<−1.27 ± 0.11	...	...	3.3
J1114+1048	$11^h14^m39^s$	+10°48′59″	4.28 ± 1.71	...	<−1.29 ± 0.12	...	...	3.2
J0843+1115	$08^h43^m31^s$	+11°15′20″	6.34 ± 2.43	...	<−1.40 ± 0.11	1.34 ± 0.07	−1.60 ± 0.40	3.2
J1015+1141	$10^h15^m39^s$	+11°41′05″	3.16 ± 1.31	...	<−1.20 ± 0.12	...	...	3.2
J0929+1133	$09^h29^m20^s$	+11°33′39″	5.71 ± 2.13	...	<−1.37 ± 0.11	1.69 ± 0.08	−1.25 ± 0.39	3.1
J1019+1405	$10^h19^m53^s$	+14°05′41″	3.69 ± 1.46	...	<−1.25 ± 0.11	0.87 ± 0.06	−1.49 ± 0.41	3.1
J1026+1431	$10^h26^m53^s$	+14°31′09″	3.96 ± 1.67	...	<−1.27 ± 0.12	...	...	3.0
J0918+1114	$09^h18^m34^s$	+11°14′45″	5.40 ± 2.24	...	<−1.36 ± 0.12	...	...	3.0

Notes. This USS sample is created by matching sources in the MWA-32T catalog with uniquely corresponding sources in the 4.85 GHz PMN catalog. Sources which have spectral indices of $\alpha < -1.2$ ($S \propto \nu^{\alpha}$) are identified as ultra-steep candidates. The sources are sorted in order of decreasing detection S/N level. MWA sources which are within 5′ of a PMN source, and have no other PMN counterparts within 30′ are matched as counterparts and used to calculate the spectral index. Additionally, for MWA sources with no PMN source within 1°, a spectral index limit is calculated using the PMN flux limit of 50 mJy. For comparison, the ultra-steep candidates are matched with MRC candidates within 15′ (sources with multiple matches within 30′ are excluded), and an additional spectral index is calculated.

a counterpart and extract a spectral index. A histogram of the spectral indices is shown in Figure 12. This histogram appears consistent with the low-frequency-selected spectral index distributions obtained by De Breuck et al. (2000), and plotted in their Figure 7 (however, the De Breuck et al. 2000 analysis used slightly different frequencies). Using a low-frequency-selected distribution results in a sample which is significantly more sensitive to the USS sources.

We choose a spectral index cutoff of $\alpha \leqslant -1.2$ for USS source candidates, and find three sources which match the criteria. All three sources have counterparts in the MRC, and the source MWA J1032−3421 has a counterpart in both the PAPER and Culgoora source lists (although the other two USS candidates do not). A further 33 sources are identified which have no counterpart in the PMN catalog within 1°. Using the PMN catalog limiting flux of 50 mJy (Griffith & Wright 1993) for these sources, we find that 25 of these 33 sources have an inferred spectral index of $\alpha \leqslant -1.2$. Of these 25 sources, 11 have unique counterparts in the MRC (one additional source has multiple counterparts), 9 have counterparts in the Culgoora source list, and none have counterparts in the PAPER source list.

A comparison between the USS source list of De Breuck et al. (2000) and the source list identified in this work finds only one source from their list which matches an MWA USS candidate within 15′: MWA J1032−3421. They select this source from an analysis of the MRC and PMN samples, and

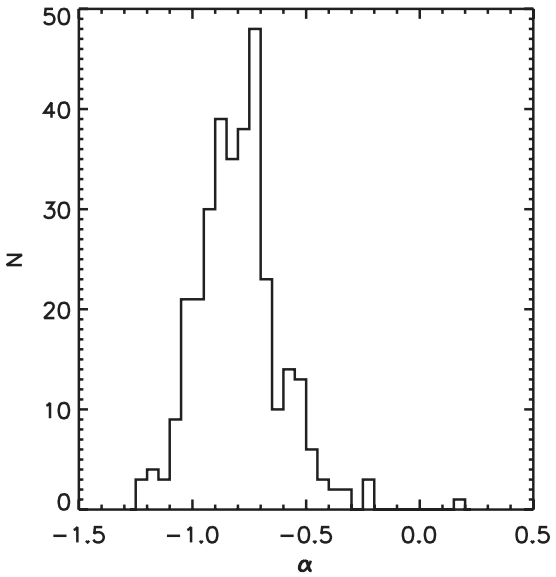

Figure 12. Distribution of spectral indices ($S_\nu \propto \nu^{\alpha}$) between 154.25 MHz and 4.85 GHz for sources identified in this paper, based on a comparison with the Parkes-MIT-NRAO catalog (Griffith & Wright 1993). To avoid issues of source confusion and blending, only sources which could be unambiguously associated with single PMN counterparts are included in the histogram.

find a spectral index of -1.23 ± 0.04, which is consistent with the MWA-32T measurements. There are an additional 21 sources from the De Breuck et al. (2000) sample which match MWA sources, however only three of these MWA sources matched uniquely with a PMN counterpart: MWA J1133−2717, MWA J0941−1627, and MWA J0937−2243. These three sources were identified as USS sources in the "TN" sample of De Breuck et al. (2000), which used measurements at 365 MHz and 1.4 GHz, but they did not meet the USS criteria in the MWA-PMN comparison. The flatter MWA-PMN spectra may indicate a high-frequency turnover in the source spectrum, similar to that noted for J0008−421 in Jacobs et al. (2011). This interpretation is supported by 74 MHz VLSS measurements of these sources (Cohen et al. 2007), which imply a spectral flattening at low frequencies, although further follow-up will be important to definitively establish this behavior.

It is important to note that these MWA sources are only candidates, and should not be treated as definitive USS sources. Flux calibration and measurement errors as well as blending issues due to the low MWA resolution and time variability may result in a reclassification of these sources upon more detailed investigation. Additionally, any time variability or errors introduced by the different catalog resolutions and fitting algorithms will add to errors in this candidate list. The MWA instrument is under continued development, and the fidelity of these studies will improve as the systematics are better understood. However, this candidate list serves as a good basis for more detailed follow-up and investigation.

8. CONCLUSIONS AND FUTURE WORK

The goals of this work were to verify the performance of the MWA subsystems and the MWA-32T system, to explore techniques for future EoR experiments, and to deepen our understanding of the radio sky at these frequencies. The analysis and results presented in this paper served to help commission MWA-32T and represent an assessment of its performance. Specifically, our ability to successfully solve for antenna gains in spite of the wide field of view and direction-dependent primary beam increases our confidence in our ability to calibrate the full 128 tile MWA array. The high level of agreement of our position measurements with existing source position measurements provides further verification of our understanding of the geometry of the array and the calibration procedures as well as our expectations for ionospheric effects on scales relevant to the MWA-32T array. In short, the high fidelity, wide-field images produced in this analysis help to build confidence that MWA will be able to achieve its design goals. The measured fluxes in the maps agree with expectations from previous catalogs with a scatter of about 30%. The magnitude of these flux residuals is similar to what is reported from other pathfinder low-frequency arrays, however it is significantly larger than expected based on the noise in the maps. Further work is needed to understand the effects that cause these flux discrepancies.

Future EoR experiments with MWA will require long integrations, which will require the combination of data from many pointings. We have shown in this work that these data can be corrected for primary beam effects and weighted averages can be formed to increase the sensitivity and fidelity of the resulting maps. In this initial exploration we made certain simplifying assumptions that allowed us to do this analysis in the image domain. Future, deeper investigations will require more sophisticated techniques that account for differences between individual antenna elements. Developing and verifying these techniques should also be a priority.

A distinguishing feature of the images presented in this paper is the degree to which they are confusion limited. The effects of source confusion are not expected to be an issue for EoR experiments. Simulations indicate, though it remains to be shown in practice, that subtracting the brightest sources, and treating the fainter sources as smooth contributors to each pixel will allow an adequate separation of foregrounds from the EoR signal (see, e.g., Liu & Tegmark 2011). For other science goals, however, it is quite clear that for the low-frequency arrays planned for the near future, the confusion limit of continuum images will be reached in relatively short integration times. Thus, much of the science will have to contend with the difficulties of measurements in crowded fields. We have presented the results of an automatic source extraction algorithm. While the results are quite good, with reliability over 90%, further development of algorithms that extract more accurate source models from crowded fields (such as the algorithm presented in Hancock et al. 2012) should be a priority.

The source list presented in this paper serves as the deepest catalog of radio sources generated from a blind search in this region of the southern sky in this frequency band and is the first MWA characterization of the EoR point-source foreground in the MWA EoR field. Further refinement of statistical descriptions of this component of the foreground should be possible, and represent a promising avenue for future work. The production of this large, high-quality survey with only ∼25 hr of data highlights the survey power of this instrument. The techniques used to survey these two fields can be extended to complete an MWA all-sky survey. It is important to note that because this survey was carried out near the source confusion limit, many of the fainter sources in the sample are likely blends of multiple sources. The USS candidates identified in this work, although likely affected by this blending, serve as a set of candidates for high-redshift radio sources, and are good targets for follow-up with higher resolution low-frequency instruments.

The MWA is in the process of a build-out to a 128 tile (128T) interferometer. The 128T array will have four times the number of collecting elements as the 32T array, and the maximum baseline length will be increased to ∼3 km. The higher resolution of the 128T array will yield maps with a lower source confusion limit, and will enable a deeper survey of this sky field with a reduced number of blended sources. With the added sensitivity, the 128T array will still be able to rapidly produce source confusion-limited maps. The techniques developed as part of the work described herein will allow evaluation of the 128T instrument as it is commissioned. As the quality of the sky model at these frequencies improves, the increased calibration accuracy and ability to subtract foregrounds from the data will move us closer toward the goal of detecting the 21 cm signal during reionization.

This scientific work uses data obtained from the Murchison Radio-astronomy Observatory. We acknowledge the Wajarri Yamatji people as the traditional owners of the observatory site. Support for this work comes from the Australian Research Council (grant Nos. LE0775621 and LE0882938), the National Science Foundation (grant Nos. AST-0457585, AST-0821321, AST-0908884, AST-1008353, and PHY-0835713), the U.S. Air Force Office of Scientific Research (grant No. FA9550-0510247), the Australian National Collaborative Research Infrastructure Strategy, the Australia India Strategic

Research Fund, the Smithsonian Astrophysical Observatory, the MIT School of Science, MIT's Marble Astrophysics Fund, the Raman Research Institute, the Australian National University, the iVEC Petabyte Data Store, the NVIDIA sponsored CUDA Center for Excellence at Harvard University, and the International Centre for Radio Astronomy Research, a Joint Venture of Curtin University of Technology and the University of Western Australia, funded by the Western Australian State government. The Centre for All-sky Astrophysics is an Australian Research Council Centre of Excellence, funded by grant CE11E0001020. The MRO is managed by the CSIRO, who also provide operational support to the MWA. This research work has used the TIFR GMRT Sky Survey (http://tgss.ncra.tifr.res.in) data products. C.L.W. thanks Adrian Liu, and Leo Stein for helpful discussions and comments, as well as the Halleen family for their hospitality at Boolardy Station while working at the MRO.

REFERENCES

Argüeso, F., González-Nuevo, J., & Toffolatti, L. 2003, ApJ, 598, 86
Baldwin, J. E., Boysen, R. C., Hales, S. E. G., et al. 1985, MNRAS, 217, 717
Bernardi, G., de Bruyn, A. G., Brentjens, M. A., et al. 2009, A&A, 500, 965
Blake, C., & Wall, J. 2002, MNRAS, 329, L37
Bock, D. C.-J., Large, M. I., & Sadler, E. M. 1999, AJ, 117, 1578
Bowman, J. D., Morales, M. F., & Hewitt, J. N. 2009, ApJ, 695, 183
Bowman, J. D., & Rogers, A. E. E. 2010, Nature, 468, 796
Broderick, J. W., Bryant, J. J., Hunstead, R. W., Sadler, E. M., & Murphy, T. 2007, MNRAS, 381, 341
Chippendale, A. P. 2009, PhD thesis, The Univ. Sydney
Cohen, A. S., Lane, W. M., Cotton, W. D., et al. 2007, AJ, 134, 1245
Condon, J. J. 1974, ApJ, 188, 279
Condon, J. J. 1997, PASP, 109, 166
Condon, J. J., Cotton, W. D., Greisen, E. W., et al. 1998, AJ, 115, 1693
Condon, J. J., Griffith, M. R., & Wright, A. E. 1993, AJ, 106, 1095
Cornwell, T. J., Golap, K., & Bhatnagar, S. 2008, IEEE J. Sel. Top. Signal Process., 2, 647
Dagkesamanskiĭ, R. D., Samodurov, V. A., & Lapaev, K. A. 2000, Astron. Rep., 44, 18
Datta, A., Bowman, J. D., & Carilli, C. L. 2010, ApJ, 724, 526
De Breuck, C., van Breugel, W., Röttgering, H. J. A., & Miley, G. 2000, A&AS, 143, 303
De Breuck, C., van Breugel, W., Stanford, S. A., et al. 2002, AJ, 123, 637
de Oliveira-Costa, A., & Capodilupo, J. 2010, MNRAS, 404, 1962
de Oliveira-Costa, A., & Lazio, J. 2010, arXiv:1004.3167
de Oliveira-Costa, A., Tegmark, M., Gaensler, B. M., et al. 2008, MNRAS, 388, 247
Di Matteo, T., Ciardi, B., & Miniati, F. 2004, MNRAS, 355, 1053
Di Matteo, T., Perna, R., Abel, T., & Rees, M. J. 2002, ApJ, 564, 576
Douglas, J. N., Bash, F. N., Bozyan, F. A., Torrence, G. W., & Wolfe, C. 1996, AJ, 111, 1945
Furlanetto, S. R., & Briggs, F. H. 2004, New Astron. Rev., 48, 1039
Furlanetto, S. R., Oh, S. P., & Briggs, F. H. 2006, Phys. Rep., 433, 181
González-Nuevo, J., Toffolatti, L., & Argüeso, F. 2005, ApJ, 621, 1
Griffith, M. R., & Wright, A. E. 1993, AJ, 105, 1666
Griffith, M. R., Wright, A. E., Burke, B. F., & Ekers, R. D. 1994, ApJS, 90, 179
Griffith, M. R., Wright, A. E., Burke, B. F., & Ekers, R. D. 1995, ApJS, 97, 347
Hales, S. E. G., Baldwin, J. E., & Warner, P. J. 1988, MNRAS, 234, 919
Hales, S. E. G., Baldwin, J. E., & Warner, P. J. 1993a, MNRAS, 263, 25
Hales, S. E. G., Masson, C. R., Warner, P. J., & Baldwin, J. E. 1990, MNRAS, 246, 256
Hales, S. E. G., Masson, C. R., Warner, P. J., Baldwin, J. E., & Green, D. A. 1993b, MNRAS, 262, 1057
Hales, S. E. G., Mayer, C. J., Warner, P. J., & Baldwin, J. E. 1991, MNRAS, 251, 46
Hales, S. E. G., Riley, J. M., Waldram, E. M., Warner, P. J., & Baldwin, J. E. 2007, MNRAS, 382, 1639
Hamaker, J. P., Bregman, J. D., & Sault, R. J. 1996, A&AS, 117, 137
Hamilton, A. J. S. 1993, ApJ, 417, 19
Hancock, P. J., Murphy, T., Gaensler, B. M., Hopkins, A., & Curran, J. R. 2012, MNRAS, 422, 1812
Harker, G., Zaroubi, S., Bernardi, G., et al. 2009, MNRAS, 397, 1138
Hogan, C. J., & Rees, M. J. 1979, MNRAS, 188, 791
Högbom, J. A. 1974, A&AS, 15, 417
Intema, H. T., van Weeren, R. J., Röttgering, H. J. A., & Lal, D. V. 2011, A&A, 535, A38
Ishwara-Chandra, C. H., Sirothia, S. K., Wadadekar, Y., Pal, S., & Windhorst, R. 2010, MNRAS, 405, 436
Jackson, C. 2005, PASA, 22, 36
Jacobs, D. C., Aguirre, J. E., Parsons, A. R., et al. 2011, ApJ, 734, L34
Kassim, N. E., Lazio, T. J. W., Erickson, W. C., et al. 2007, ApJS, 172, 686
Lane, W. M., Clarke, T. E., Taylor, G. B., Perley, R. A., & Kassim, N. E. 2004, AJ, 127, 48
Large, M. I., Mills, B. Y., Little, A. G., Crawford, D. F., & Sutton, J. M. 1981, MNRAS, 194, 693
Lidz, A., Zahn, O., McQuinn, M., Zaldarriaga, M., & Hernquist, L. 2008, ApJ, 680, 962
Liu, A., & Tegmark, M. 2011, Phys. Rev. D, 83, 103006
Liu, A., Tegmark, M., Bowman, J., Hewitt, J., & Zaldarriaga, M. 2009, MNRAS, 398, 401
Lonsdale, C. J., Cappallo, R. J., Morales, M. F., et al. 2009, IEEE Proc., 97, 1497
Madau, P., Meiksin, A., & Rees, M. J. 1997, ApJ, 475, 429
McQuinn, M., Zahn, O., Zaldarriaga, M., Hernquist, L., & Furlanetto, S. R. 2006, ApJ, 653, 815
Mitchell, D. A., Greenhill, L. J., Wayth, R. B., et al. 2008, IEEE J. Sel. Top. Signal Process., 2, 707
Morales, M. F., & Hewitt, J. 2004, ApJ, 615, 7
Morales, M. F., & Wyithe, J. S. B. 2010, ARA&A, 48, 127
Nayak, A., Daiboo, S., & Shankar, N. U. 2010, MNRAS, 408, 1061
Oberoi, D., Matthews, L. D., Cairns, I. H., et al. 2011, ApJ, 728, L27
Ord, S. M., Mitchell, D. A., Wayth, R. B., et al. 2010, PASP, 122, 1353
Paciga, G., Chang, T.-C., Gupta, Y., et al. 2011, MNRAS, 413, 1174
Pandey, V. N. 2006, PhD thesis, Raman Research Institute
Parsons, A. R., Backer, D. C., Foster, G. S., et al. 2010, AJ, 139, 1468
Pedani, M. 2003, New Astron., 8, 805
Pen, U.-L., Chang, T.-C., Hirata, C. M., et al. 2009, MNRAS, 399, 181
Pritchard, J. R., & Loeb, A. 2011, Prog. Rep. Phys., in press (arXiv:1109.6012)
Rengelink, R. B., Tang, Y., de Bruyn, A. G., et al. 1997, A&AS, 124, 259
Rottgering, H. J. A., Braun, R., Barthel, P. D., et al. 2006, in Cosmology, Galaxy Formation and Astroparticle Physics on the Pathway to the SKA, ed. H. R. Klockner, S. Rawlings, M. Jarvis, & A. Taylor (Dwingeloo: ASTRON), 169
Schwab, F. R. 1984, AJ, 89, 1076
Scott, D., & Rees, M. J. 1990, MNRAS, 247, 510
Shaver, P. A., Windhorst, R. A., Madau, P., & de Bruyn, A. G. 1999, A&A, 345, 380
Sirothia, S. K., Kantharia, N. G., Ishwara-Chandra, C. H., & Gopal-Krishna., 2011, The GMRT Sky Survey, http://tgss.ncra.tifr.res.in/
Slee, O. B. 1977, Aust. J. Phys. Astrophys. Suppl., 43, 1
Slee, O. B. 1995, Aust. J. Phys., 48, 143
Swarup, G., Ananthakrishnan, S., Kapahi, V. K., et al. 1991, Curr. Sci., 60, 95
Tasker, N. J., Condon, J. J., Wright, A. E., & Griffith, M. R. 1994, AJ, 107, 2115
Wilman, R. J., Miller, L., Jarvis, M. J., et al. 2008, MNRAS, 388, 1335
Wright, A. E., Griffith, M. R., Burke, B. F., & Ekers, R. D. 1994, ApJS, 91, 111
Wright, A. E., Griffith, M. R., Hunt, A. J., et al. 1996, ApJS, 103, 145
Zhang, X., Zheng, Y., Chen, H., et al. 1997, A&AS, 121, 59